

THE PENNSYLVANIA STATE UNIVERSITY
SCHREYER HONORS COLLEGE

DEPARTMENT OF BIOENGINEERING

**FINITE ELEMENT ANALYSIS OF MICROFABRICATED POLY(GLYCEROL
SEBACATE) SCAFFOLDS FOR HEART VALVE TISSUE ENGINEERING**

SURJYANIL CHOWDHURY

Spring 2012

A thesis
submitted in partial fulfillment
of the requirements for a baccalaureate degree
in Bioengineering
with honors in Bioengineering

©2012 Surjyanil Chowdhury
April 2012

The thesis of Surjyanil Chowdhury was reviewed and approved* by the following:

William Hancock
Associate Professor of Bioengineering
Thesis Advisor

Peter Butler
Associate Professor of Bioengineering
Honors Advisor

Keefe Manning
Associate Professor of Bioengineering

* Signatures are on file in the Schreyer Honors College.

ABSTRACT

Heart valve tissue engineering has the potential to make artificial valves which can grow, self-repair, and produce a minimal immune response when implanted due to being constructed of the patients own cells. In this study, finite element analysis using COMSOL multiphysics was used to examine the capability of microfabricated poly(glycerol sebacate) (PGS) scaffolds to both mimic the anisotropic behavior of native valvular tissue and to support collagenous tissue formation. This approach of using finite element (FE) analysis to model and analyze PGS scaffolds which could then be optimized based on the model was a novel approach used to study the structural mechanics of a recently developed PGS scaffold. This scaffold was comprised of diamond pores prior to and after cell seeding the constructs. Specifically, 2-D FE models of PGS scaffolds and cell seeded scaffolds were generated to predict the effective stiffness of the scaffold and engineered tissue.

Experimental data of stiffness (done by the lab and generated from uniaxial mechanical tester samples) was matched with the stiffness obtained from FE analysis of representative scaffolds for two orthogonal material directions (PD along the long axis of the diamond pore and XD along the short axis of the pore). The findings indicated that the microfabricated PGS scaffold had mechanical characteristics which follow a rule-of-mixtures (corrected for angle) behavior. Furthermore, FE analysis was used to develop a correlation between the scaffold's pore geometry and strut width (within the fabrication design) and the scaffold's stiffness to determine an appropriate design that mimics the native leaflet's stiffness and anisotropy. Results showed that the scaffold increased in anisotropy as the angle of the diamond shaped pore diverged from 90° when the overall volume fraction of the scaffold was held constant as the angle changed. Finally, uniaxial mechanical testing data on cell seeded scaffolds (done by the lab) was used to model a cell seeded scaffold that was used to predict the stiffness of the tissue formed within the scaffold.

TABLE OF CONTENTS

ACKNOWLEDGEMENTS.....	iii
Chapter 1: INTRODUCTION.....	1
1.1 Artificial Heart Valves Currently Used Clinically.....	2
1.2 Implication of Tissue Engineering.....	2
1.3 Engineering TEHV Scaffolds	4
1.4 Previous Finite Element (FE) Modeling of TEHV	5
1.5 Use of FE in the Current Study.....	5
Chapter 2: METHODS	7
2.1 Theoretical Calculation Using Rule of Mixtures	7
2.2 Two Dimensional Finite Element Model.....	9
2.3 Experimental Mechanics Testing of PGS Scaffold.....	15
Chapter 3: RESULTS & DISCUSSION.....	17
3.1 Comparison of Theoretical, Finite Element, and Experimental Models.....	17
3.2 Correlation Between Pore Geometry and Scaffold Stiffness	24
3.3 Cell Seeded Scaffold Model and Tissue Formation.....	26
Chapter 4: CONCLUSIONS, LIMITATIONS, AND FUTURE EXPERIMENTS.....	30
REFERENCES	32
APPENDICES	34
Appendix A: Equations used by COMSOL Multiphysics	34
Appendix B: Step-by-Step FE Model Explanation.....	36
Appendix C: FE Results with Meshing	41

ACKNOWLEDGEMENTS

I would like to acknowledge my thesis advisor, Dr. William Hancock, for helping me develop this study, proofreading, and approving this thesis; my honors advisor Dr. Peter Butler for proofreading and approving this thesis; Dr. Keefe Manning for proofreading and approving this thesis; Dr. George Engelmayr Jr. for his assistance in developing this study; and graduate student Nafiseh Masoumi for her experimental research and data referred to in this thesis as “the lab,” her assistance in developing this study, and for proofreading this thesis.

Chapter 1: INTRODUCTION

Designed by surgeon Dr. Charles A. Hufnagel in 1952, the first artificial heart valve (AHV) was a plastic caged-ball valve which was inserted into the thoracic aorta, immediately distal to the left subclavian artery [Fig. 1]. At the time, implantation of this artificial heart valve was a ground breaking surgical procedure that actively sought to treat aortic insufficiency and congestive heart failure by correcting a hemodynamic defect: the abnormal blood flow occurring within the heart and its surrounding arteries, specifically the aorta. The artificial valve mechanically reduced the

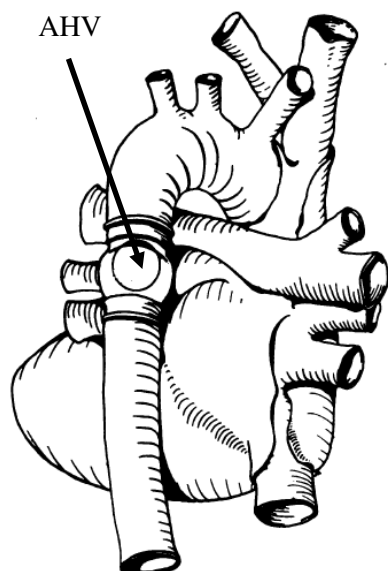


Figure 1: Sketch of Hufnagel AHV and placement in the thoracic aorta [1].

volume of blood reentering that heart through regurgitant flow [1]. However, since the Hufnagel AHV did not replace the diseased aortic valve and was a mechanical heart valve, it could not integrate into the patient's body and did not completely cure the patient's aortic insufficiency.

Since clinical application of the plastic caged-ball heart valve, more than fifty different artificial heart valves have been designed and over three million AHV's have been implanted worldwide [2]. From 2008, the demand for artificial heart valves has been expanding 10-12% per year. The AHV industry has been a lucrative business, producing a need for more advanced heart valve replacements which can essentially replace diseased valves. Ideally, a replacement heart valve should be able to mimic the mechanical properties of the native aortic valve; be able to integrate into the body seamlessly without the formation of thrombosis and scar tissue or incitation of a negative immune response; and be able to remodel with the body. Currently, mechanical heart valves and bioprosthetic heart valves are in clinical use.

1.1 Artificial Heart Valves Currently Used Clinically

The most commonly used mechanical heart valve, which accounts for approximately 80% of implanted mechanical valves, is the bileaflet mechanical heart valve [2]. This AHV improved on the previous mechanical heart valve (caged-ball) design by reducing occluder-induced turbulence in blood flow through and distal to the valve and overall was a more compact design. However, many pitfalls remained with the mechanical heart valve design, mainly being thrombosis occurring near the valve with the possibility of embolizing and anticoagulant-related bleeding resulting from patients having to take anticoagulation drugs orally which prevent thrombosis [3]. To overcome these drawbacks, artificial heart valves were created from naturally occurring heart valves including porcine xenograft valves; bovine pericardial valves; and allograft or homograft valves [2, 4]. Despite many redesigns of both mechanical and bioprosthetic heart valves, current AHV's are still plagued with issues of structural valvular deterioration, non-structural dysfunction, thrombosis, embolism, bleeding, and endocarditis [5]. There is now a high demand for a functional artificial heart valve that overcomes these drawbacks and essentially replaces the diseased valve.

1.2 Implication of Tissue Engineering

The field of tissue engineering presents a possible solution to the previously mentioned dilemma by proposing an AHV created by seeding the patient's own cells within a scaffold. The scaffold would structurally mimic the native valvular tissue and degrade over time as the patient's body remodels the implanted tissue. Since the implant is created with the patient's own cells, it is hypothesized that this type of implant would likely reduce negative immunologic responses and be easily integrated into the patient's body [6]. However, it is necessary that this assumption also include the scaffolding material used to create the mechanical structure necessary to promote cell proliferation and extracellular matrix (ECM) formation. Tissue engineered heart valves (TEHV) have potential but many challenges remain before considering clinical applications and human implantation. A usable TEHV is predicted to be a complex model composed of different cells

and ECM that remodel in response to changes in local mechanical forces and changes in TEHV composition as healing occurs [6]. This usable TEHV would also need to mimic the mechanical properties of the native valve (being flexible and durable) from the initial implantation of the TEHV, throughout the healing and remodeling process as the scaffold degrades and is replaced by the patient's own cells and ECM, and over time years after implantation.

As previously mentioned, the scaffold used for the functional TEHV should mimic native leaflet anisotropic mechanical properties at the time of implantation and during the remodeling process. The scaffold should also promote cell growth, proliferation, and ECM formation while it slowly degrades as collagen fibers replace the scaffolding material. Synthetic scaffolds have shown to have many limitations; for example as seen in Figure 2 taken by Engelmayr et al., nonwoven scaffolds do not produce uniform pores [7]. It is difficult to see the two orthogonal directions clearly (PD and XD) due to the nonuniformity of the structure. It is also more difficult to control the mechanics of such a structure for this same reason (nonuniformity). A similar result occurs with electrospun fibers. Combining the precision of microfabrication with cardiac bio-mimicry, Engelmayr

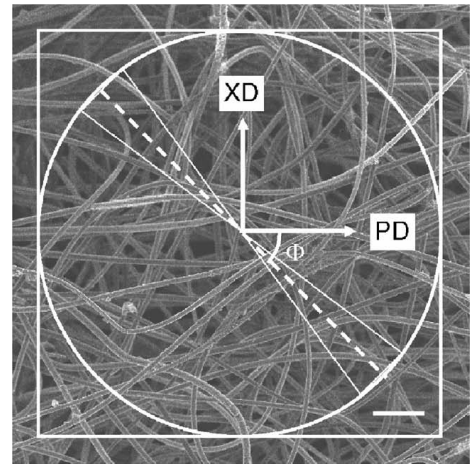


Figure 2: Picture of nonwoven poly glycolic acid scaffold taken by Engelmayr et al [7].

et al. developed an accordion-like honeycomb poly(glycerol sebacate) (PGS) scaffold toward replicating aspects of cardiac structural mechanics [8]. This scaffold consisted of uniform pore density and pore geometry. In the study carried out for this thesis, PGS scaffolds were computationally designed and laser microfabricated by the lab to match the anisotropy and peak tangent Young's modulus of bovine native heart valve leaflets. This study not only tested new scaffold pore geometry (with diamond shaped pores) but also achieved a cell-seeded model that could be used to predict tissue stiffness and ECM content within cell-seeded constructs. This study was also carried out in an effort to understand the mechanics of this new scaffold with the

diamond shaped pores by quantifying the effects of pore geometry on the stiffness of the scaffold. By understanding the effects of the pore geometry on scaffold stiffness, the computational models could be modified and be used to develop a pore geometry that produces scaffold stiffness similar to that of native valve leaflet tissue.

1.3 Engineering TEHV Scaffolds

Based on previous research done by Hammer et al., heart valve leaflets exhibit an anisotropic, nonlinear stress–strain relationship that undergoes large deformations under physiological loads [9]. Although the TEHV are composites of living tissue and synthetic scaffold material, the effective mechanical property of the TEHV is initially dictated by the scaffold’s mechanical property, which is relatively stiffer than the seeded cellular material. This property is consistent within the body as ECM and the collagen network accounts for most of the structural mechanics within a tissue rather than the actual mechanics of the cells. However, the overall goal with tissue engineering heart valves has been the following: to obtain tissue formation regardless of the scaffolds presence, to create a mechanically stable scaffold that exhibits the native heart valve leaflet mechanical properties; and to create a cell-seeded construct that has the same architecture and function as the native tissue [10]. Therefore, during the *in vitro* cultivation time and early stage of implantation, the synthetic scaffold would still be intact. This means that the TEHV effective mechanical properties are influenced by both the scaffold and ECM contributions, mainly from collagen fibers, during this initial stage before implantation and during the early implantation phase.

Optimizing the mechanical properties of scaffolds is becoming more feasible with the help of mathematical and computational modeling such as FE analysis. In 2005, Engelmayer et al. developed a composite beam model that accounts for the effects of nonwoven scaffold-extracellular matrix (ECM) and variations in collagen concentration [11]. The model was then used to predict the effective stiffness in the ECM of TEHV samples incubated under static and

cyclic flexure conditions. In the study for this thesis, a similar approach was used to model a PGS scaffold containing uniform diamond shaped pores using finite element analysis.

1.4 Previous Finite Element (FE) Modeling of TEHV

Many published studies used mathematical modeling as well as finite element (FE) analysis on computational models to study normal, pathological, and prosthetic valves [12]. Other FE models have been created to evaluate the mechanical interaction of native valve leaflets in relation to the surrounding physiological environment [9, 12]. However, few studies, based on computational or theoretical modeling, were devoted to predict the strength and stiffness of biomaterials used in tissue engineering [11, 13]. In a recent study done by Jean et al., finite element 2-D simulations on a homogeneous scaffold were used to predict the anisotropic effective stiffness of an accordion-like honeycomb (ALH) shaped PGS scaffold [13]. Based on the approach used by Jean et al., the study done for this thesis used FE to analyze a PGS scaffold containing uniform diamond shaped pores.

1.5 Use of FE in the Current Study

In this study, microfabricated PGS scaffolds comprised of diamond shape pores, were generated by the lab using a micromodeling technique [14]. Tensile mechanical testing, on scaffolds and cell seeded scaffolds, was conducted to define the mechanical properties of the samples. Using the commercially available simulation software COMSOL Multiphysics, 2-D representative models of two material directions (preferred (PD) and orthogonal cross-preferred (XD)) were generated. Finite element simulations were used to predict the anisotropic effective stiffness of the PGS scaffolds. First, the elastic moduli and associated anisotropy obtained by FE simulations were compared to the effective stiffnesses measured by uniaxial mechanical testing of PGS scaffolds cured for 12 hrs at 160°C by the lab. These were also compared to results obtained from theoretical calculations using the rule-of-mixtures equation after being corrected for the angle of the pore [8]. Following this step, the diamond-shaped pore geometry parameters were

changed in the simulations to depict the correlation between the scaffolds stiffness and pore geometry parameters. This correlation was intended to assist in experimental scaffold microfabrication design which would result in a scaffold with mechanical properties matching native tissue stiffness and anisotropy. Finally, the stiffness of tissue formation following 4 weeks cultivation of valvular interstitial cells (VIC) was predicted using FE analysis for the composite material. The stiffness of the tissue formation was also predicted for native bovine aortic heart valve tissue. By using FE analysis as a prediction tool, TEHV constructs can ideally be made that have the specific characteristics of native heart valve tissue.

Chapter 2: METHODS

For the first part of the study, a theoretical calculation of scaffold stiffness (using rule of mixtures corrected for the angle) was compared to FE analysis results and experimental results. FE was then used to correlate scaffold geometry to the stiffness of the PGS scaffold material. Finally, a composite cell seeded scaffold model was made using FE to predict the stiffness of the tissue formed within the scaffold, and the results were compared to native bovine aortic valvular tissue.

2.1 Theoretical Calculation Using Rule of Mixtures

The simple rule of mixtures for a composite material model (corrected for angle) was used to estimate the scaffold's stiffness by knowing the volume fraction of the PGS material in the scaffolds (calculated from the FE model). In this case, the scaffold's struts were considered fibers that were cross-linked, being 27.9° with respect to PD (angle α in Fig. 3). The void stiffness was set as zero in equation 1. This angle of 27.9° was also calculated from the FE model and based off of the measurements of scaffold dimensions for the scaffolds used in the experimental phase. The stiffness of the tissue formed inside the scaffold pores was considered homogenous and assessed based on this model as well. A theoretical stiffness of the composite cell-seeded scaffold was then calculated.

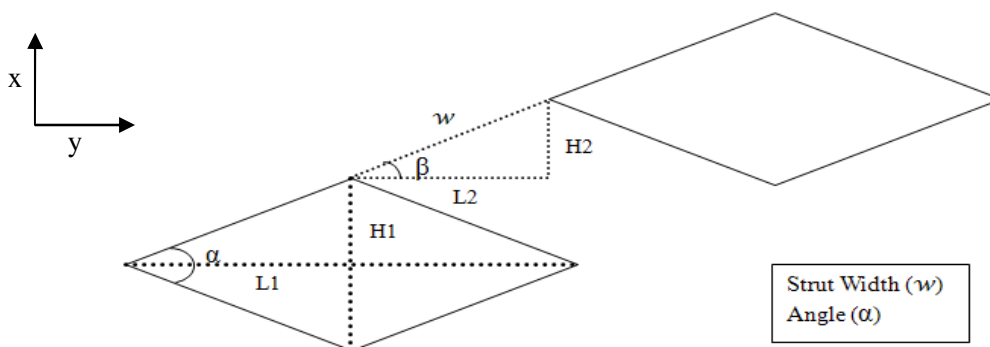


Figure 3: Sketch of pore geometry and distances used to produce FE models. Angle α and strut width w were modified within the geometry testing experiments. L1 describes $\frac{1}{2}$ of the long axis of the diamond pore and H1 describes $\frac{1}{2}$ of the short axis of the diamond pore. Angle β is equal to $\frac{1}{2}$ of angle α and was used to calculate the distances the pores were apart (L2 and H2). L2 is the distance in the x-direction that the pores were apart and H2 is the distance in the y-direction that the pores were apart.

The general equation of effective stiffness of a composite material based on scaffold fiber alignment and composite volume fraction is:

$$E = n_0 E_f v_f + E_m (1 - v_f) \quad (1)$$

$$n_0 = \sum \alpha_i \cos^4 \theta_i \quad (2)$$

Where E is the effective stiffness of the composite material (cell seeded scaffolds), E_f is the effective stiffness of the scaffold's fiber (in this case the scaffold's struts), and E_m is the effective stiffness of the tissue matrix (note that E_m is zero when considering just a scaffold model since the pores are void space). The volume fraction of the scaffold is v_f and n_0 is a corrective factor for the angle of polymer fibers with respect to the loading axis. In this case n_0 was defined by the angle of struts with respect to the loading axis, as defined by the geometry of the diamond shaped pores (Fig. 3). For a composite comprised of unidirectionally oriented structural members, $n_0 = 1$, and for a scaffold comprised of randomly oriented fibers it is 0.375 [8]. For our geometry, $\theta_i = 27.9^\circ$, which led to:

$$n_0 = 0.5 \cos^4(27.9^\circ) + 0.5 \cos^4(-27.9^\circ) = 0.61 \quad (3)$$

Based on this correction factor, a theoretical stiffness was calculated for the PGS scaffold with the diamond shaped pore geometry, and the result were compared to FE simulation and experimental results.

2.2 Two Dimensional Finite Element Model

To predict the PGS scaffold's elastic stiffness, models with 7 mm length, 4 mm width, and 0.25 mm thickness were generated matching the size of experimental samples. The 2-D models were simulated based on ESEM pictures of the microfabricated scaffolds taken by the lab (Fig. 4). Although both a 3-D and 2-D model were made, FE analysis was continued using the 2-D model with a constant 0.25 mm thickness to simplify the model and reduce processing time. This simplification was allowable since the loading and strain analysis of the scaffolds was done uniaxially in the x-direction, the load being constantly distributed in the z-direction. The first FE model depicted the strut width and pore geometry specific in the scaffolds used in the experimental analysis. This model was used to derive a stiffness of the scaffold in the PD and XD directions for comparison with the theoretical and experimental results.

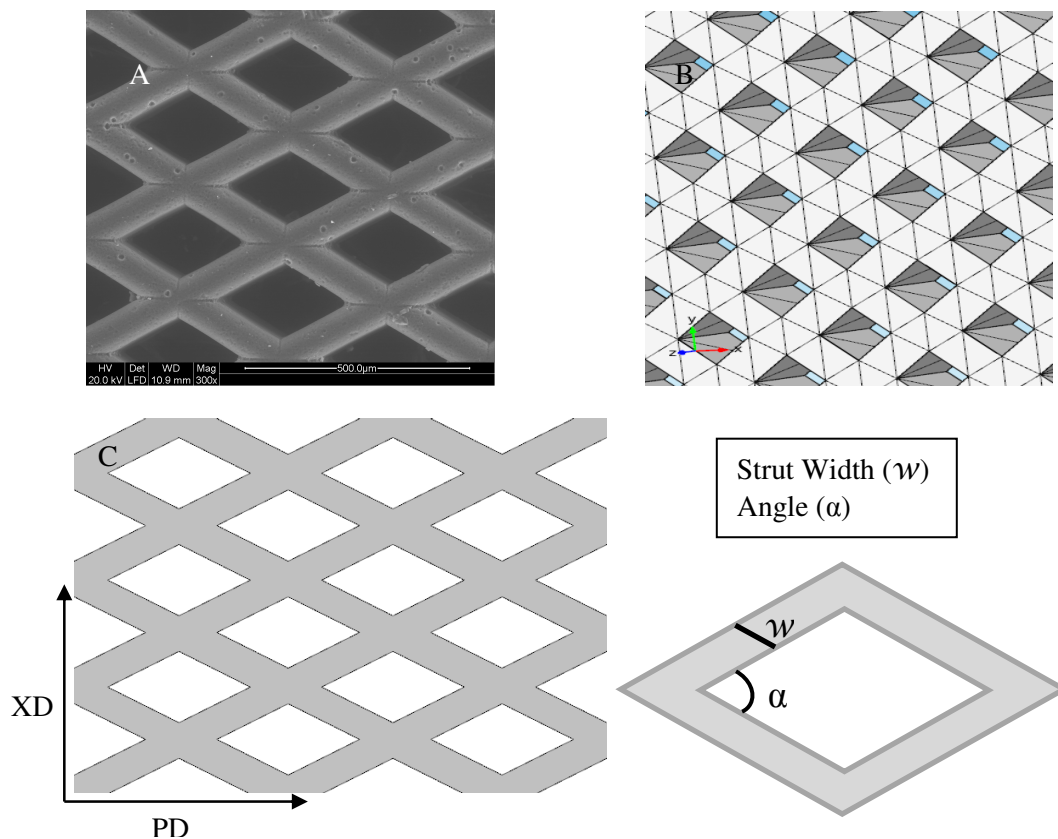


Figure 4: Enlarged images of center section of the scaffold in a SEM image of the scaffold (A), 3-D FE model of scaffold with meshing (B), and 2-D FE model showing the PD and XD directions and pore geometry defined by strut width (w) and angle (α) (C). Image A was taken by the lab during the experimental testing of the scaffold.

As seen in Figure 3, pore geometry defined by strut width (w) and angle (α) was defined in the FE model by lengths L1, H1, L2, and H2. A strut width (w) of 65 μm was used in the first model to match experimental scaffold geometry. Angle (α) was calculated based off known measurements for L1 (122.5 μm) and H1 (65 μm) that were also measured from the experimental data by Nafiseh Masoumi. Using similar triangles, the values L1 and H1 were then calculated from the angle β .

Table 1: Calculations for pore geometry based on similar triangle analysis and known geometries taken from experimental results. The measurements of L1, H1, L2, and H2 were used to make the pores for the FE models.

Angle (α) degrees	Angle (β) degrees	Angle (β) radians	Hyp1 (μm)	L1 (μm)	H1 (μm)	Strut Width (w)	L2 (μm)	H2 (μm)
30	15.0	0.3	200	193.2	51.8	35	33.8	9.1
						50	48.3	12.9
						60	58.0	15.5
						70	67.6	18.1
45	22.5	0.4	200	184.8	76.5	35	32.3	13.4
						50	46.2	19.1
						60	55.4	23.0
						70	64.7	26.8
65	32.5	0.6	200	168.7	107.5	35	29.5	18.8
						50	42.2	26.9
						60	50.6	32.2
						70	59.0	37.6
90	45.0	0.8	200	141.4	141.4	35	24.7	24.7
						50	35.4	35.4
						60	42.4	42.4
						70	49.5	49.5

In order to relate the scaffold's stiffness to the pore geometry and strut width, 16 sets of scaffolds (both PD and XD models) with different pore geometries (i.e. diamond angle $\alpha = 30, 45, 65, 90^\circ$) and strut widths (35, 50, 60, 70 μm) were modeled and analyzed using FE (see Table 1 for calculations of geometry). Similar to the scaffold models, light microscopic pictures taken by the lab of the cell seeded samples were used to design the models of the cell seeded scaffolds (Fig. 5). A homogenous material was considered inside the diamond pores for simplicity. As shown in the confocal images taken by the lab (Fig. 5a) following 4 weeks VICs cultivation on the fabricated scaffolds, tissue formation appears inside the diamond pores; the effective mechanical behavior of the tissue was computed with FE analysis based on this experimental data.

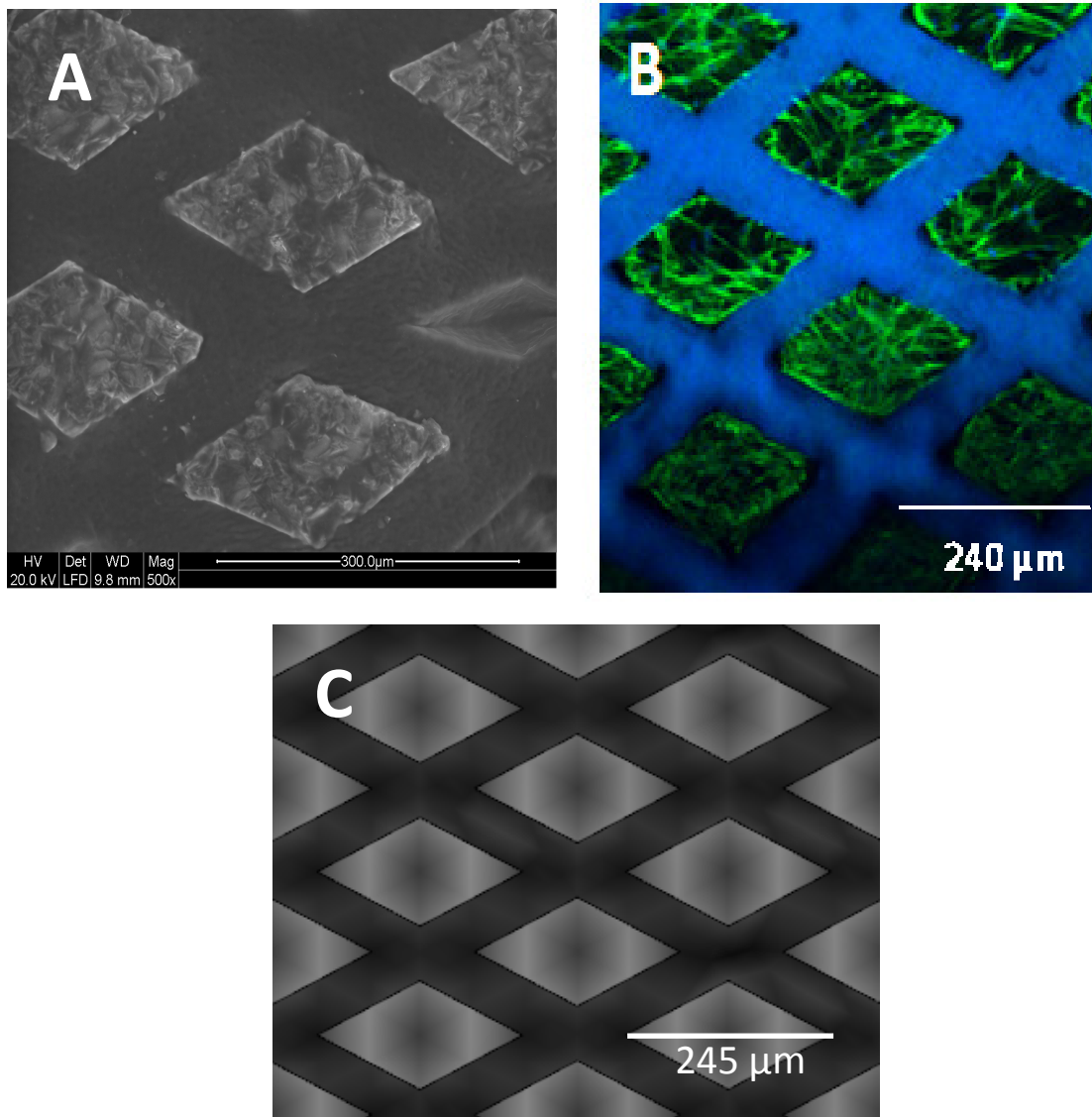


Figure 5: Cell seeded scaffold following 4 weeks of cultivation light microscopic image (A), confocal image (B), and 2-D FE model image (C). A depiction of the free-triangular mesh used can be seen in Figure 8. Images A and B were taken by the lab during the experimental testing of the cell-seeded scaffold.

The PGS structural elements were assumed to exhibit isotropic linear elastic behavior based on uniaxial mechanical tester results completed in the lab. For the PGS material, the Young's modulus was assigned as 1.77 MPa based on the uniaxial tensile testing of PGS membranes, cured for 12 hrs and soaked in 60°C water overnight, done by Masoumi in the lab. A Poisson's ratio equal to 0.49 was also assumed for the scaffolds structure. The 2-D models of the scaffolds representing the PD and XD samples were considered fixed from the left edges and stretched

through the length from the right edge according to uniaxial tensile tests (Fig. 6). Various loads ranging from 0 to 0.3 N/m^2 were applied to the right edge when testing the models. For each described value of applied stress, the corresponding strain value was measured and the linear curve of the stress-strain was plotted to measure the stiffness of the scaffolds for the two orthogonal PD and XD directions.

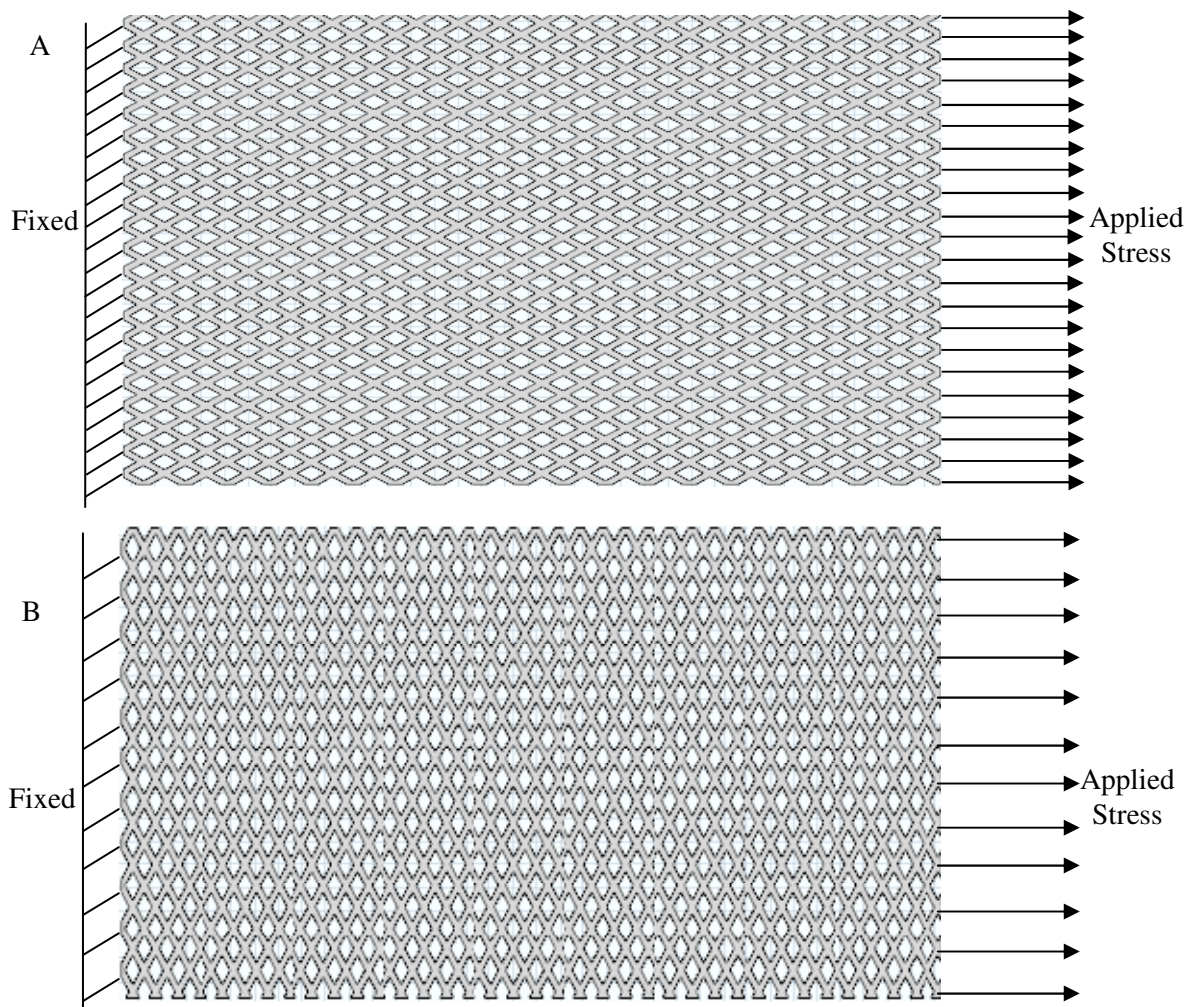


Figure 6: Diagram of applied loads in the 2-D FE models for PD (A) and XD (B) oriented diamond pores.

Strain was specifically calculated from the measured displacement of the right edge of the model. To quantify the influence of fabrication design dimensions (pore geometry and strut width) similar simulations were done to predict the effective stiffnesses and anisotropy (EPD and EXD) for a range of diamond pore angles (α) and strut widths (w) as specified in Table 1. To compute

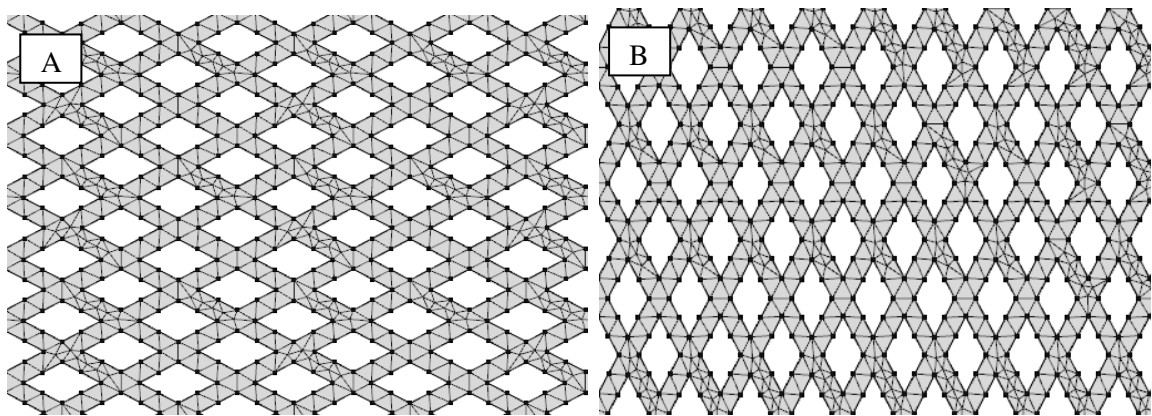
the effective stiffness, the equations (described in Appendix A) were used to relate the measured stress and strain values.

Finally, the model of a cell seeded scaffold generated from light microscopy images was analyzed for predicting the stiffness of tissue formation inside the scaffold's pores and estimating collagen content within the composite scaffolds. The tissue formation within the void spaces was assumed homogenous, which exhibits isotropic linear elastic behavior similar to the PGS structure when considering loading in only one direction (either the x or the y direction). The effective stiffness of the cell-seeded scaffolds (obtained from the initial linear part of the experimental stress-strain curve) was adjusted to the mechanical property of the composite model (the tissue) in the FE material properties. The effective stiffness of the tissue formed inside the pores was predicted by plotting various Young's moduli of the tissue (ranging from 30 kPa to 120 kPa) versus Young's moduli of the overall composite construct (calculated from the FE analysis). This curve could then be used to calculate the stiffness of the experimental composite scaffold's tissue formation. Note that for this cell seeded model, a Young's modulus of 1.3 MPa was used for the PGS material to match experimental results, and a density of 1060 kg/m^3 and Poisson's ratio of 0.49 were used for the tissue [15]. A step-by-step explanation of how the FE models were made can be seen in Appendix B. The meshing within the models was tested, showing that a fine free-triangular mesh with the parameters listed in Table 2 kept the data the most consistent between models (see Table 2 for a summary of all the parameters used in the FE modeling). Images of the FE models of the scaffold and the cell-seeded scaffold with pores oriented in either the PD or XD direction can be seen in Figures 7 and 8 with meshing. Meshing and results of example models used in the geometry testing experiments can be seen in Appendix C. As seen in Appendix C, the density of the mesh (the number of triangles per unit area of the scaffold) decreased as angle α increased, and the density of the mesh decreased as strut width increased.

Table 2: Parameters used in the FE model for the scaffold geometry, material properties, and mesh.

Parameter	Value
Scaffold Geometry	
Length	7mm
Width	4mm
Height	0.25mm
Scaffold Material Properties	
Young's Modulus	1.77MPa
Poisson's Ratio	0.49
Density	1235
Mesh	
Max Element Size	400
Min Element Size	2.1
Resolution of curvature	0.3
Resolution of narrow regions	1

Figure 7 shows the free-triangular mesh used for the scaffold models in the PD (A) and XD (B) pore orientations. Notice that the pores, the void space, were plain white indicating that no material was present within these areas. These images were taken of the center of the scaffold which had a pore angle α of 27.9° (with respect to the PD direction) and a strut width of $65\ \mu\text{m}$.

**Figure 7:** Models of scaffold with free-triangular meshing with pores oriented in the PD (A) and XD (B) directions.

Parameters for the mesh can be seen in Table 2.

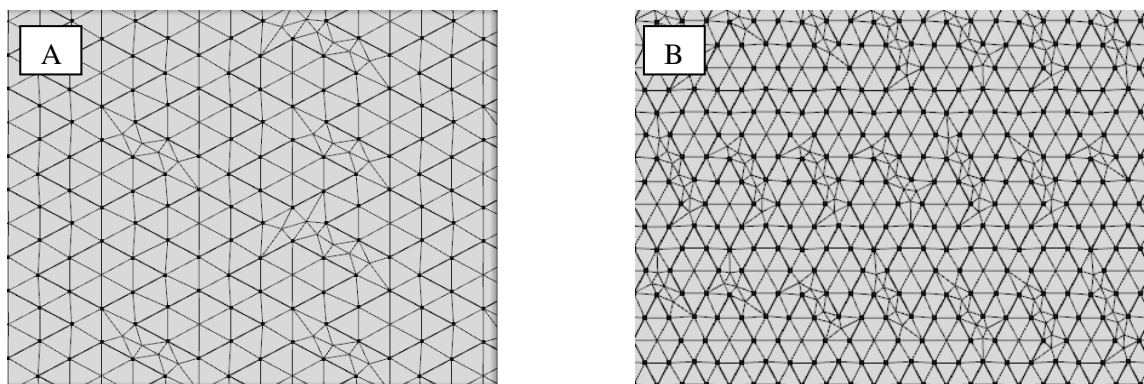


Figure 8: Models of cell-seeded scaffold with free-triangular meshing with pores oriented in the PD (A) and XD (B) directions. Parameters for the mesh can be seen in Table 2.

Figure 8 shows the free-triangular mesh used for the cell-seeded scaffold models in the PD (A) and XD (B) pore orientations. As seen in the mesh, the same mesh was used for the tissue and scaffold regions in order to achieve uniformity between the two regions (so that COMSOL would see the two areas as connected within the mesh). Note that the images were of the center of the cell-seeded scaffold which had a pore angle α of 27.9° (with respect to the PD direction) and a strut width of $65\ \mu\text{m}$.

2.3 Experimental Mechanics Testing of PGS Scaffold

The experimental methods regarding PGS synthesis, scaffold microfabrication and cell seeding and cultivation process were previously published and are detailed briefly below. Note that the experimental part of this study was done by graduate student Nafiseh Masoumi within the lab. In brief, PGS polymer was synthesized by a method adapted from Wang et al. [14], reacting glycerol and sebacic acid (1:1 molar ratio, Sigma) under heat (120°C) and N_2 for 24 hrs, followed by 24 hrs high vacuum ($\sim 15\ \text{mTorr}$) to yield a viscous pre-polymer. PGS was fabricated by a new micro-molding process on the ceramic molds (ultra-high temperature machinable glass-mica ceramic sheet (0.5" thick, $2" \times 2"$, McMaster) using a dicing cutter machine. Pre-polymer was melted on a mold and was cured in a vacuum oven (160°C and 12 hrs; a PGS Young's modulus

of 1.43 MPa.) yielding scaffolds comprised of approx. 2:1 aspect ratio diamond shape pores and about 65 μm strut width.

Cell seeding techniques have also been described previously in detail. Briefly, VIC were isolated from fresh porcine heart valve leaflets by overnight digestion in a solution of 0.2% (w/v) type I collagenase (Worthington Biochemical) in HBSS at 37°C. Following expansion, porcine aortic VIC were seeded onto PGS microfabricated scaffolds overnight at a density of 2×10^6 cells/cm² in 12 mL of media in sterile vented 50 cc bioreactor tubes (TPP, Trasadingen, Switzerland) that were placed in a rotisserie rotator (Thermo-Fisher, Pittsburgh, PA). VIC-seeded scaffolds (XD and PD samples) were cultivated statically in 4mL of the standard culture medium supplemented with 82 $\mu\text{g/mL}$ L-ascorbic acid-2-phosphate in 6-well Costar Ultralow Attachment plates (Corning) for a time period of 4 weeks. Additional micromolded PGS scaffolds and the VIC-seeded scaffold were prepared and subjected to uniaxial tensile testing (LLOYD) as described previously [13].

Chapter 3: RESULTS & DISCUSSION

Based on the experimental results, 2-D FE models for the PGS scaffold with the diamond shaped pore geometry and cell-seeded scaffold were generated. The FE models were used to calculate the volume fraction and the stiffness of the scaffolds. The model was first used to confirm experimental and theoretical (rule of mixtures) results of the scaffold stiffness. The scaffold pore geometry was then modified to develop a correlation between pore angle (α), strut width (w), and scaffold stiffness. Finally, a graph of the stiffness of tissue formation versus the overall stiffness of the composite construct was generated from FE results of a cell-seeded scaffold which was then used to predict the stiffness of the tissue formed within the pores.

3.1 Comparison of Theoretical, Finite Element, and Experimental Models

From the previously mentioned parameters, a 2-D FE model was made using the dimensions of the experimental scaffold. Using a surface integration function within the model, volume fraction was calculated as 0.557 for the PD oriented scaffold and 0.558 for the XD oriented scaffold. These volume fractions were used to generate the theoretical stiffness from the rule of mixtures equation. As seen in Table 3, the stiffness of the PD scaffold was comparable between the FE and experimental results (with 0.34% difference). For the XD direction, the FE and experimental results were less comparable (with 34% difference). For both pore orientations, the theoretical model was not very comparable to both the FE and experimental results, meaning that a more accurate theoretical model is needed for this specific PGS scaffold construct.

Table 3: Stiffness of PGS scaffold for FE and theoretical results and stiffness, ultimate tensile strength, and strain to failure for experimental results for both the PD and XD pore orientations

	FEM	Theoretical	Experimental		
	E (MPa)	E (MPa)	E (MPa)	UTS	ϵ_f
PD	0.879	0.600	0.876 ± 0.0656	0.250 ± 0.059	0.422 ± 0.0325
XD	0.194	0.0474	0.128 ± 0.0982	0.0902 ± 0.0192	0.474 ± 0.0864

Note that the values of the experimental data shown in Table 3 were averages for 3 separate trials. Figure 9 shows a graphical representation of the best fit of the experimental data to the FE analysis results (stress vs. strain). The trends were quite linear, especially in the FE results. This linear trend indicated that the FE model was correctly showing a stress-strain correlation between simulations of various applied loads since the relationship was linear when considering the peak tangent of the data as the material was stretched. As expected, the FE model provided a more linear fit than the experimental results. The slopes within this stress-strain curve indicate the Young's moduli or effective stiffness of the scaffold. Between the FE and experimental results, the Young's moduli were quite comparable (with 0.79% difference for PD and 4.6% difference for XD). Note that the PD oriented scaffold samples had a better fit between the FE and experimental results than the XD oriented scaffolds.

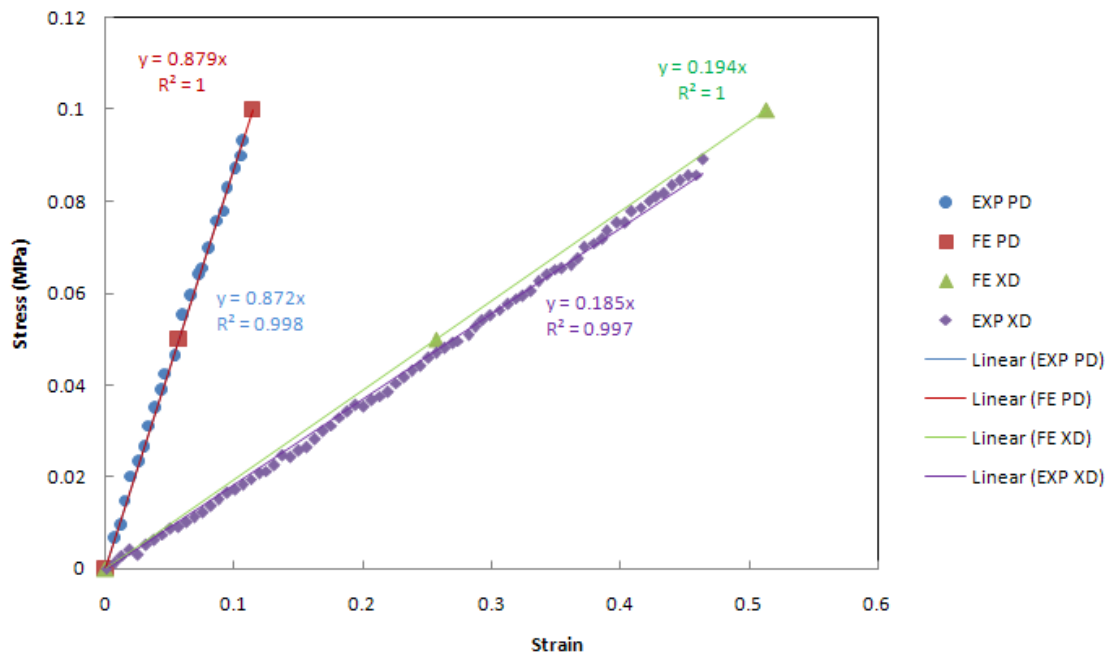
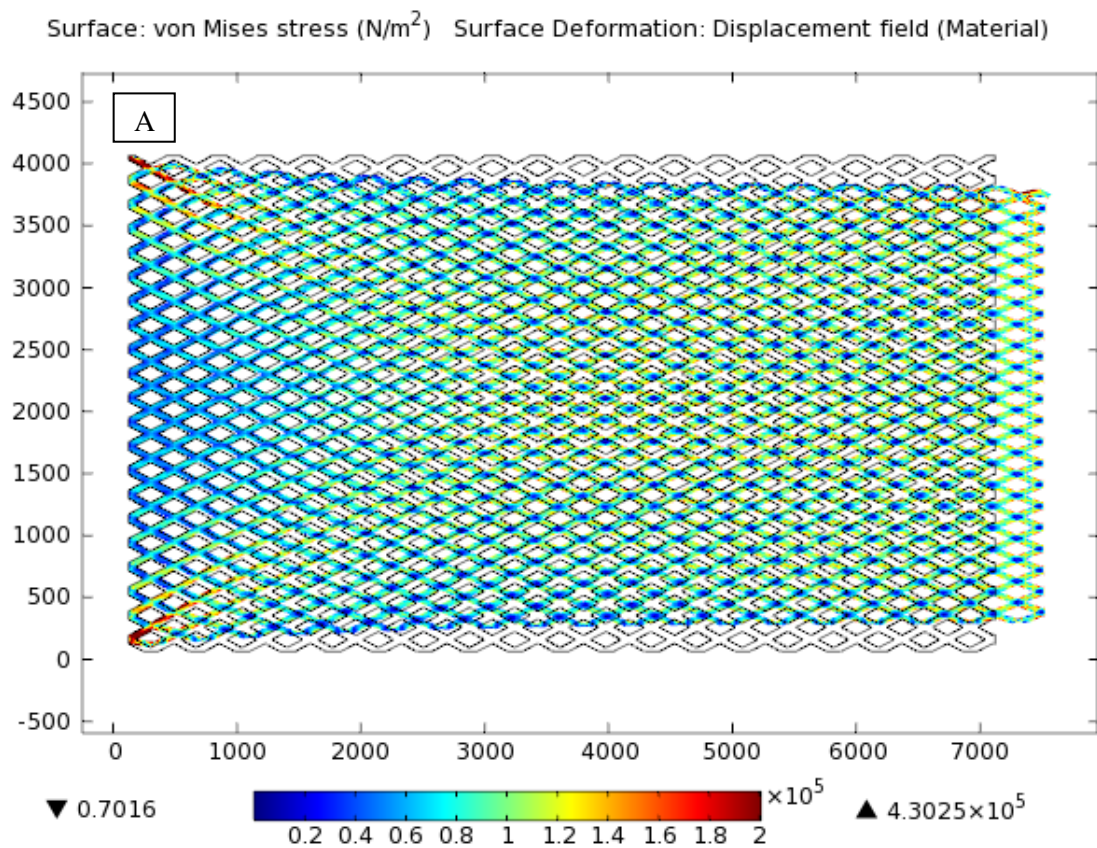


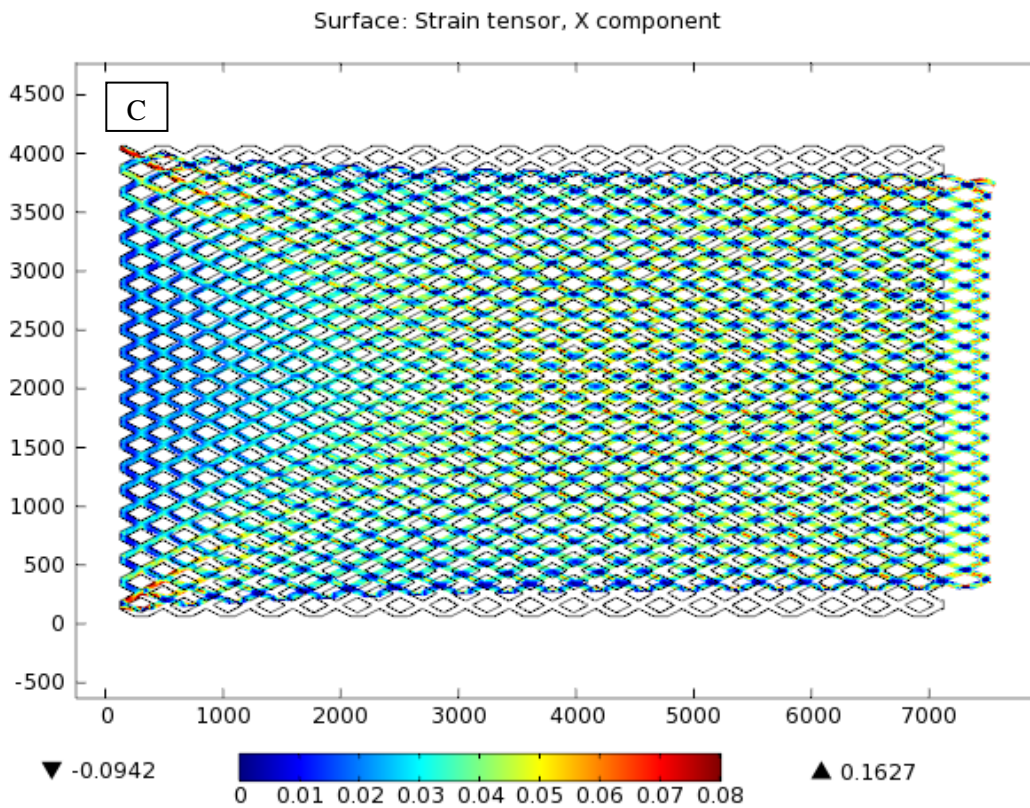
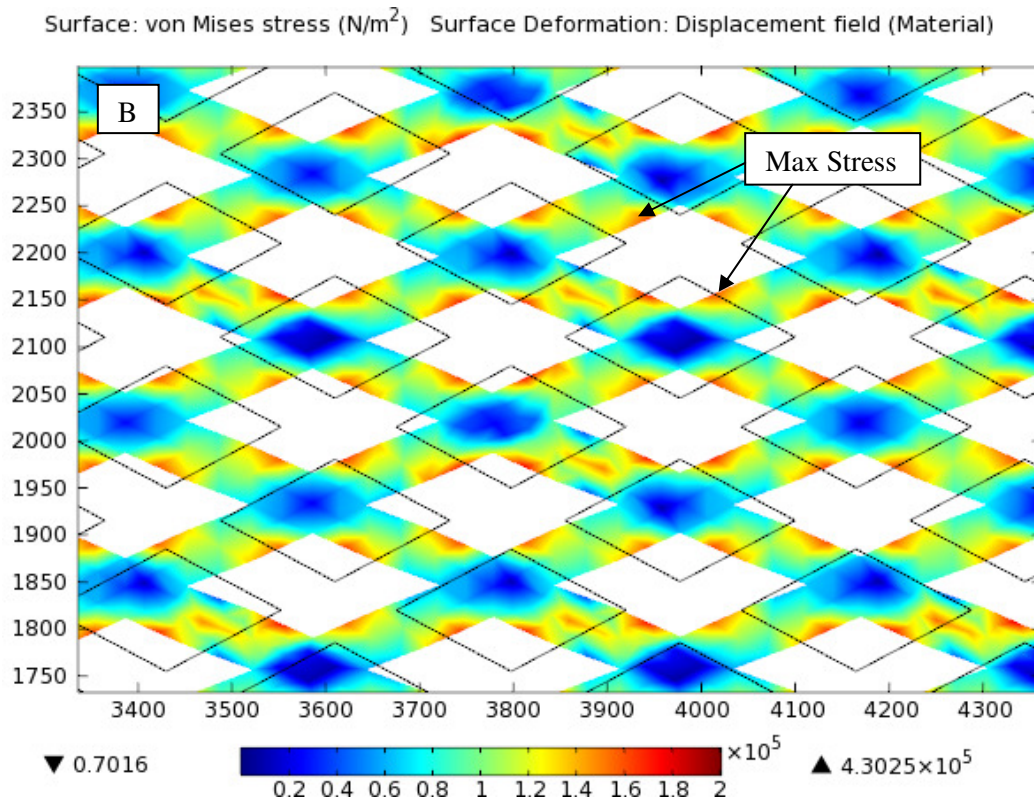
Figure 9: Stress-strain curve for the best fit of experimental data and FE results for both PD and XD pore orientations. The plot shows linear trend lines which fit the data well.

Regarding the two pore orientations, it is evident in the theoretical, FE, and experimental results that the PD pore orientation produced a higher stiffness within the scaffold when compared to the XD pore orientation. This result indicates that the larger angle α within the XD oriented pores

allows for a greater displacement within the material as a load is applied. The difference in the stiffnesses with these two directions indicates an overall anisotropic behavior within the scaffold. The material, however, can be considered isotropic when only considering the x-direction.

FE results for this 2-D scaffold using a 0.1MPa load can be seen in Figure 10 (PD) and Figure 11 (XD). As shown, the maximal stress and strain in both cases was seen in the middle of the strut. This result agreed with what was expected since the scaffolds were the most compliant at the connection points and produced the greatest stresses and strains at the stiffer strut regions. A clearer, zoomed-in image of the deformation occurring as the scaffold stretches can be seen in Figures 10 B,D and 11 B,D. As seen in these zoomed in images of the center of the scaffold, deformation occurs in both the x and y directions. The deformation or shrinking of the scaffold in the y direction occurred in order to account for the deformation (and material displacement or stretching) occurring in the x-direction.





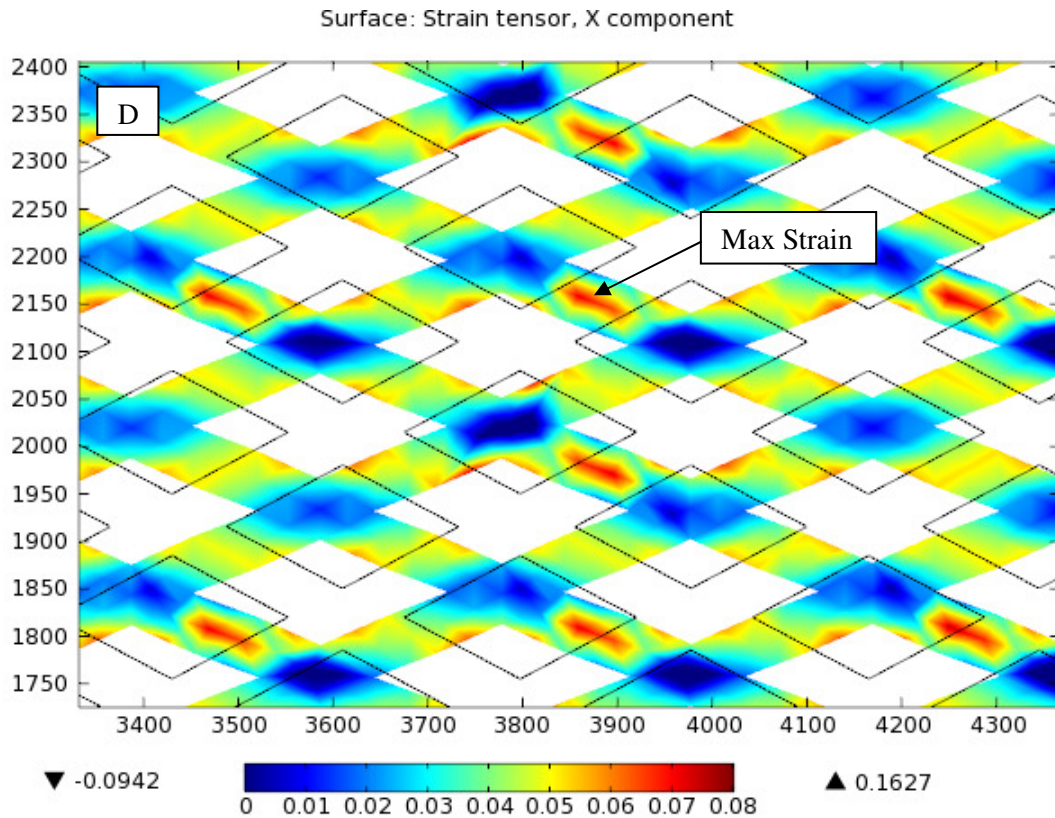
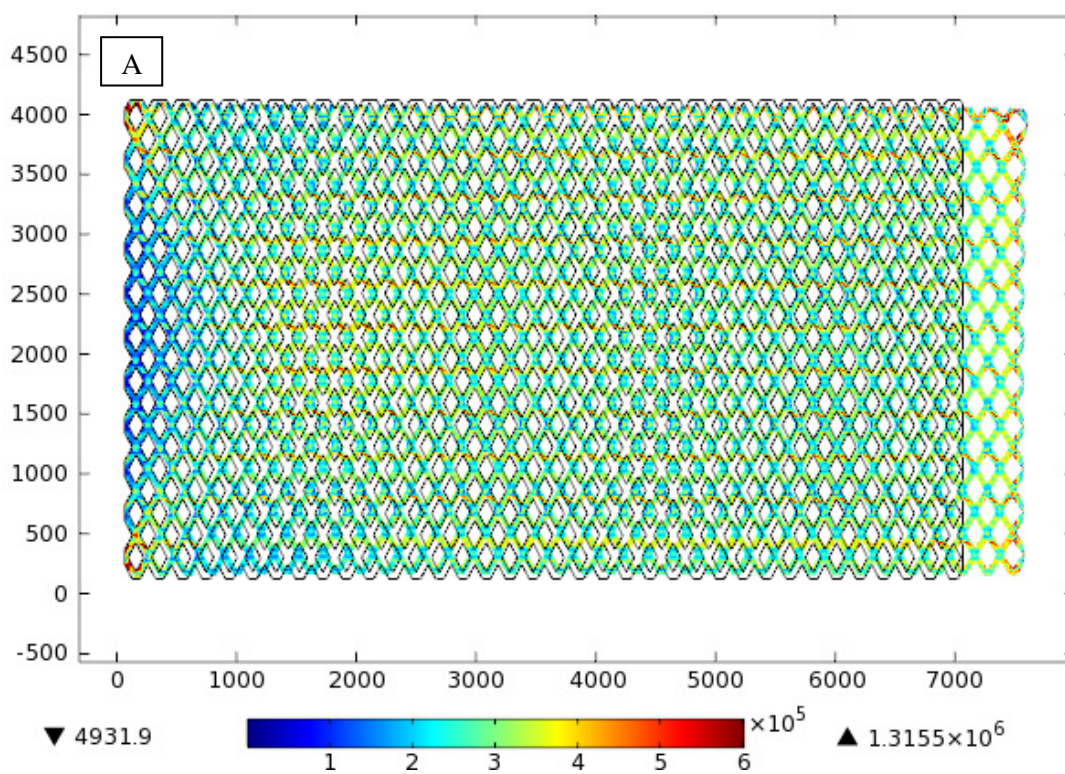
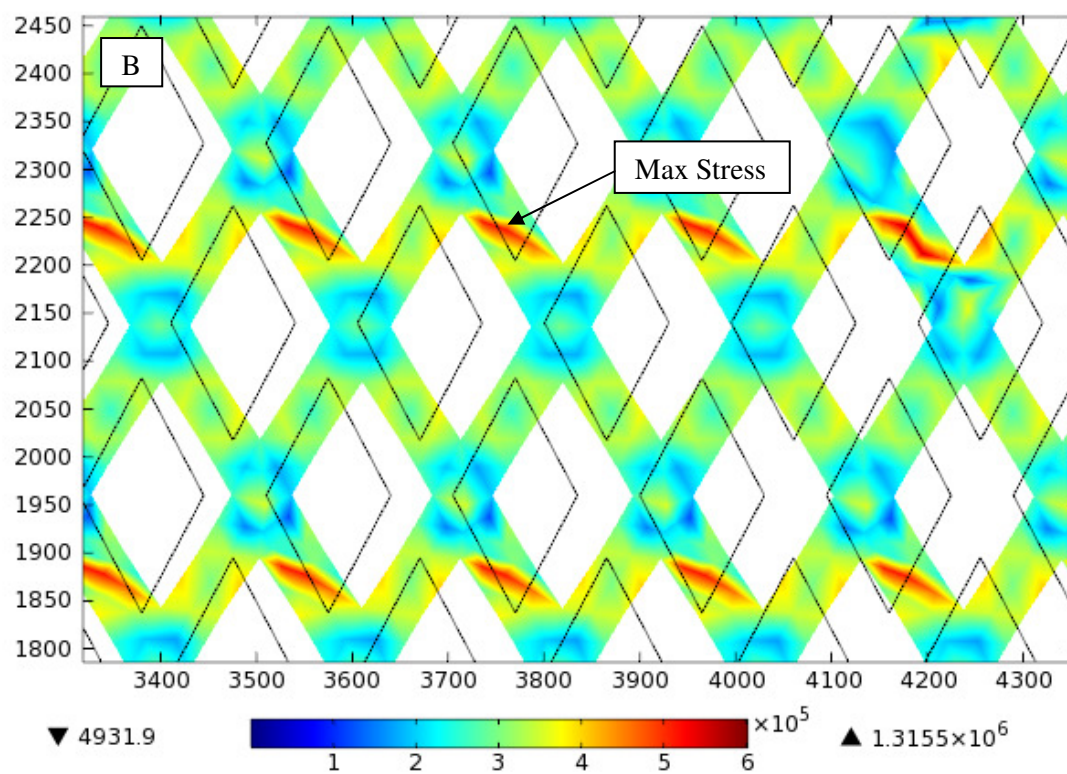


Figure 10: Stress (A, B) and strain (C, D) distributions for PD scaffold stretched using a 0.1MPa load. (A) shows the overall von Mises stress distribution within the PD scaffold and (B) shows a zoomed-in image (center of the scaffold) of the stress, showing the deformation occurring. Similarly, (C) shows the overall strain distribution in the x-direction within the PD scaffold and (D) shows a zoomed-in image (center of the scaffold) of the strain, showing the deformation that is occurring. Note that the deformation shows that the scaffolds displace in both the x and y directions. As the scaffold is stretched in the x-direction, it shrinks in the y-direction to account for the displacement in the x-direction. This effect can also be seen below in the XD models. The models were done for a pore geometry with an angle α of 27.9° and a strut width of $65\ \mu\text{m}$.

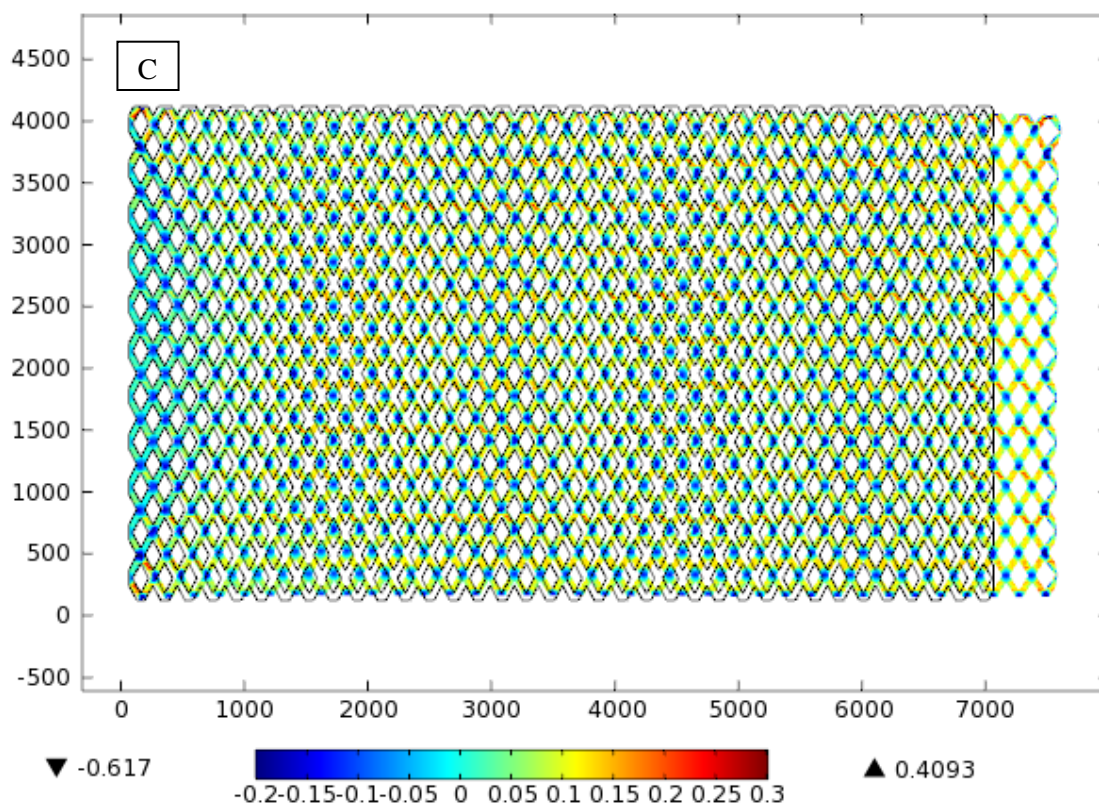
Surface: von Mises stress (N/m²) Surface Deformation: Displacement field (Material)



Surface: von Mises stress (N/m²) Surface Deformation: Displacement field (Material)



Surface: Strain tensor, X component



Surface: Strain tensor, X component

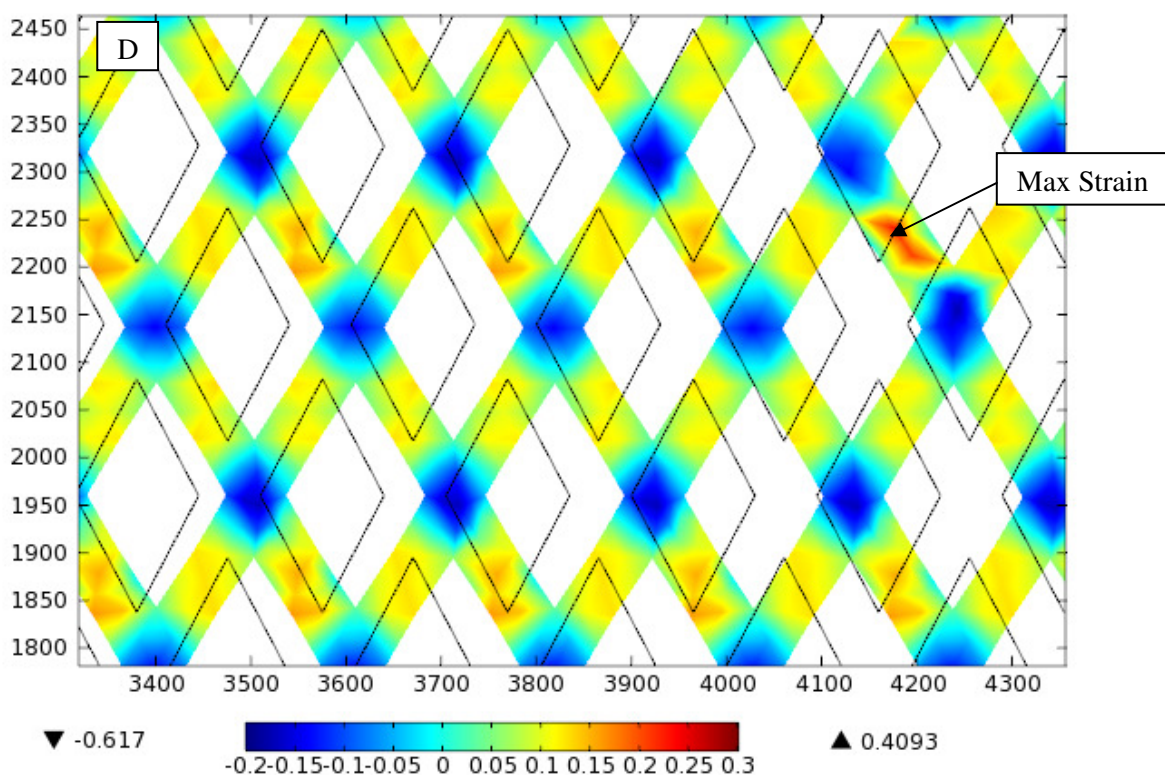


Figure 11: Stress (A, B) and strain (C, D) distributions for XD scaffold stretched using a 0.1MPa load. (A) shows the overall von Mises stress distribution within the XD scaffold and (B) shows a zoomed-in image (center of the scaffold) of the stress, showing the deformation occurring. Similarly, (C) shows the overall strain distribution in the x-direction within the XD scaffold and (D) shows a zoomed-in image (center of the scaffold) of the strain, showing the deformation that is occurring. Similar to the PD models, the deformation shows a displacement in the y-directions due to the scaffold shrinking in the y-directions in order to accommodate for the displacement in the x-direction. However, this deformation is less noticeable in the XD models when compared to the PD models.

3.2 Correlation Between Pore Geometry and Scaffold Stiffness

As previously mentioned, this part of the study was also carried out in an effort to understand the structural mechanics of this new scaffold with the diamond shaped pores by quantifying the effects of pore geometry on the stiffness of the scaffold. The computational models could later be modified and be used to develop a pore geometry that produces scaffold stiffness similar to that of native valve leaflet tissue based on the results discussed below.

To be consistent within the experiment, volume fraction was maintained as a constant as the inner angle of the pore was changed. As seen in Figure 12, volume fraction was only dependent on the change in strut width and increased as strut width increased. The volume of the PGS scaffold did not change as the angle changed because as the angle α would increase, the volume of the pores would increase, but the number of pores in the scaffold would decrease. The increase in pore volume decreased the volume of the PGS scaffold; however the reduction in the number of pores had the opposite effect, so overall the volume of the PGS scaffold was maintained constant regardless of the angle (Fig. 12B).

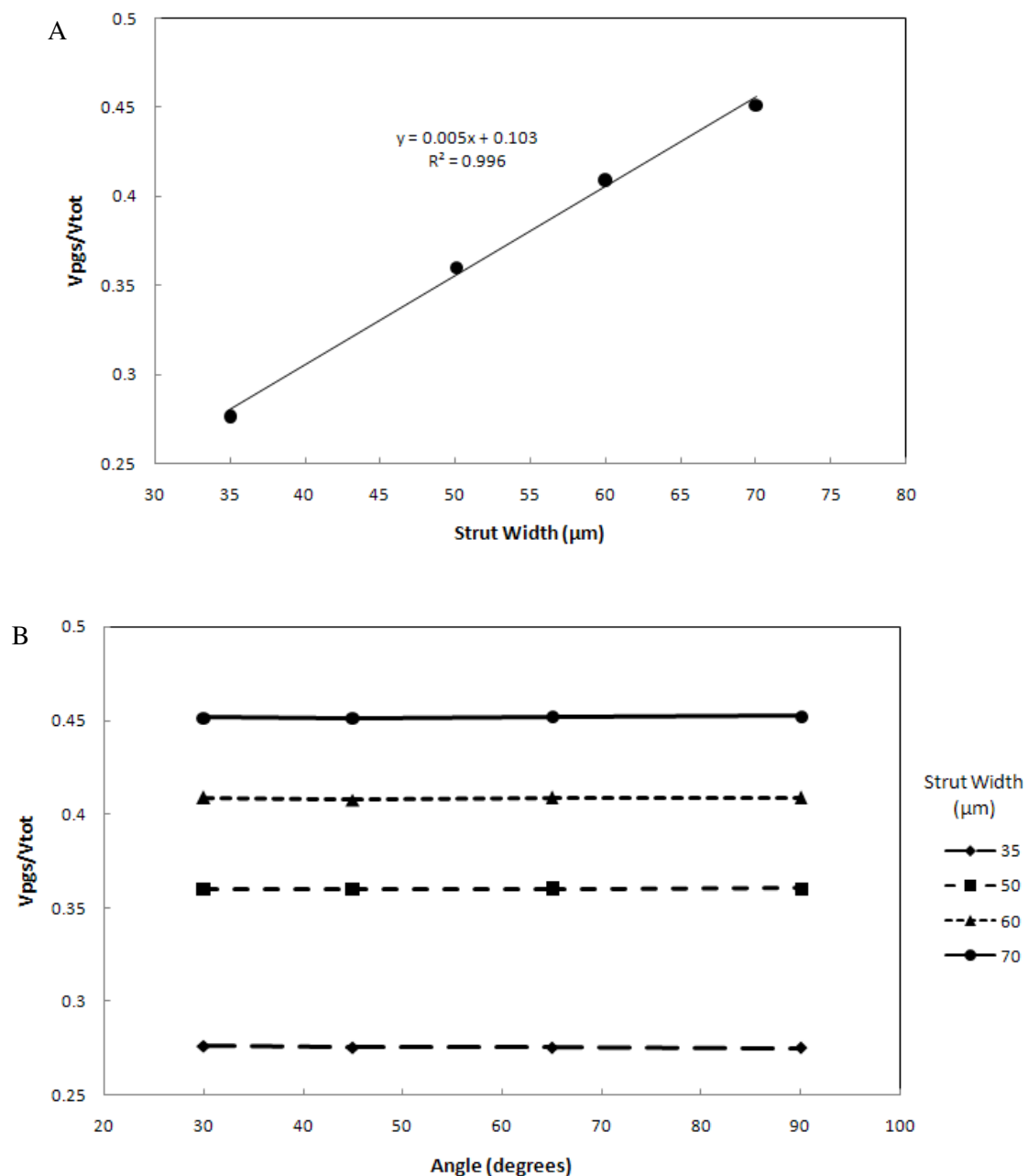


Figure 12: Volume fractions of PD oriented scaffold as strut with changes (A) from 35 to 70 μm . Volume fraction data was the same for XD pore orientation. As evident in the graph, volume fraction was constant as angle α changed (B) from 30° to 90°. Volume fraction was only dependent on strut width.

To test the anisotropy of the scaffold, the angle α was changed from 30° to 90° and the stiffness of the scaffold was measured in both the PD and XD directions (EPD and EXD). The ratio between these two stiffnesses (EPD/EXD) gave an idea of the anisotropic behavior of the scaffold with this geometry. As the scaffold becomes more isotropic, the expected ratio of EPD/EXD approaches 1.

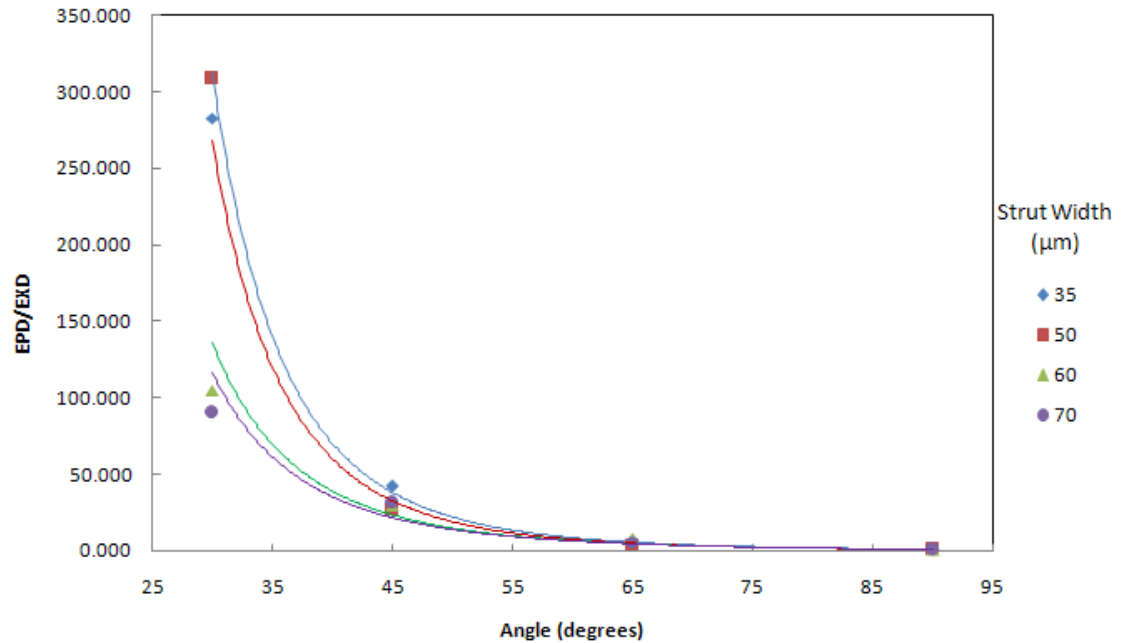


Figure 13: Correlation between the ratio EPD/EXD to angle α showing a decrease in anisotropy as the angle approached 90° . The curves are the best fit trends for the data and are solely meant to visually show the trend in the data.

As seen in Figure 13, the scaffold increased in anisotropy as the angle α decreased (the highest ratio of EPD/EXD being seen at an angle of 30°). The trend did continue past 30° (data not shown but 15° was seen to be even higher in EPD/EXD ratio). Also as seen in Figure 13, the change in strut width had less of an effect on the anisotropy of the material as the angle approached 90° . Strut width tended to affect the material stiffness more when the angle was reduced. Overall, the anisotropy of the material was dictated by the angle of the diamond pore (α) when the volume fraction was only affected by a change in strut width.

3.3 Cell Seeded Scaffold Model and Tissue Formation

After testing the PGS scaffold model using FE, a cell seeded model was developed based on light microscopy images of a cell-seeded scaffold (taken by Masoumi). The tissue formation within the void spaces in the model was assumed homogenous and isotropic when loading uniaxially in one direction. The effective stiffness of the tissue formed inside the pores was predicted by plotting various Young's moduli of the tissue (ranging from 30 kPa to 120 kPa) versus Young's

moduli of the overall composite construct (calculated from the FE analysis). For future experiments, this curve will be used to calculate the stiffness of the experimental composite scaffold's tissue formation. Images of the FE models of the scaffold and the cell-seeded scaffold with pores oriented in either the PD or XD direction can be seen in Figure 8 with meshing.

This model has the most relevance to the application of this scaffold in tissue engineering as it can be used to predict tissue formation occurring within the pores. As seen in Figure 14, FE was used to test various Young's moduli of the tissue formation occurring within the pores. Changing this Young's modulus resembles a change in the stiffness of the pore which would occur due to a change in the cell number or the ECM formation. The structural mechanics of the tissue and its stiffness are affected more by the ECM formation and the collagen fiber network.

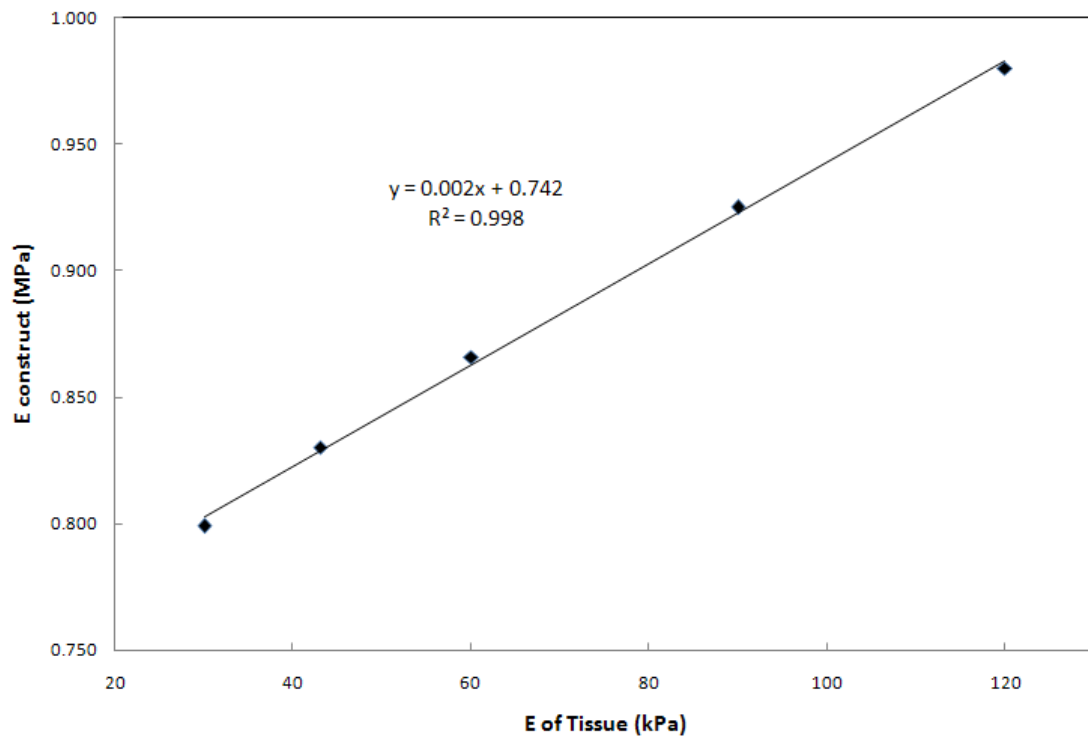
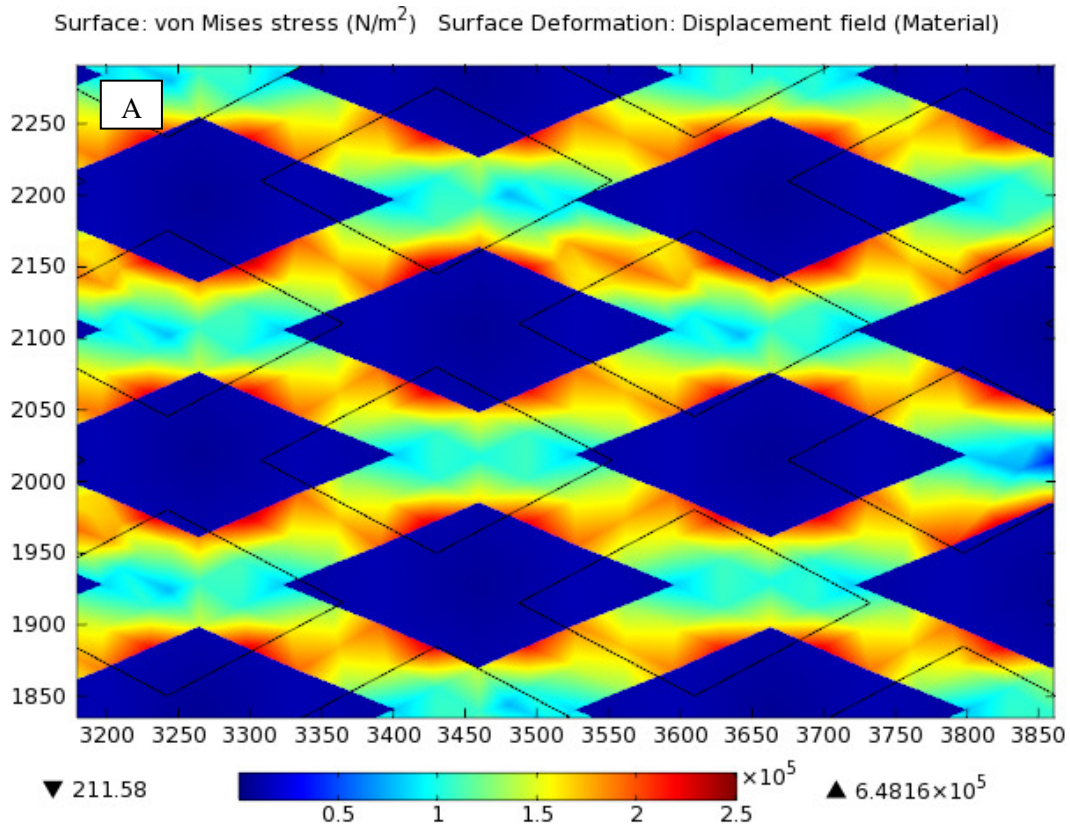


Figure 14: Correlation between E of tissue formed inside pores and E of overall composite seeded scaffold. The relationship is linear, showing the stiffness of the composite increases as the stiffness of the forming tissue increases. The stiffness of the tissue increases as seeded scaffolds are cultivated (as the number of cells and extracellular matrix formation both increase).

The stiffness of the scaffold used to generate the results of Figure 14 was equal to 1.3 MPa (note that this value was measured for the scaffolds used in the experimental phase of the cell-seeded scaffolds by Masoumi, unpublished). This stiffness would need to be changed specifically for each PGS scaffold made since the stiffness of the scaffolds is not always constant and depends on not only on the pore geometry and strut width but also the curing time. Specifically for a 1.3 MPa PGS scaffold, Figure 14 demonstrates the stiffness of the tissue forming within the pores if we measure the overall stiffness of the composite experimentally. For native bovine valvular tissue, a stiffness of 0.848 ± 0.37 MPa was measured by the lab. According to Figure 14, if we were to seed these cells on a 1.3 MPa PGS scaffold, the tissue would need to grow until the stiffness of the tissue was 52.83 kPa. Our overall construct would have a stiffness of 0.848 MPa (matching the native tissue) if the stiffness of the tissue formed was 52.83 kPa.



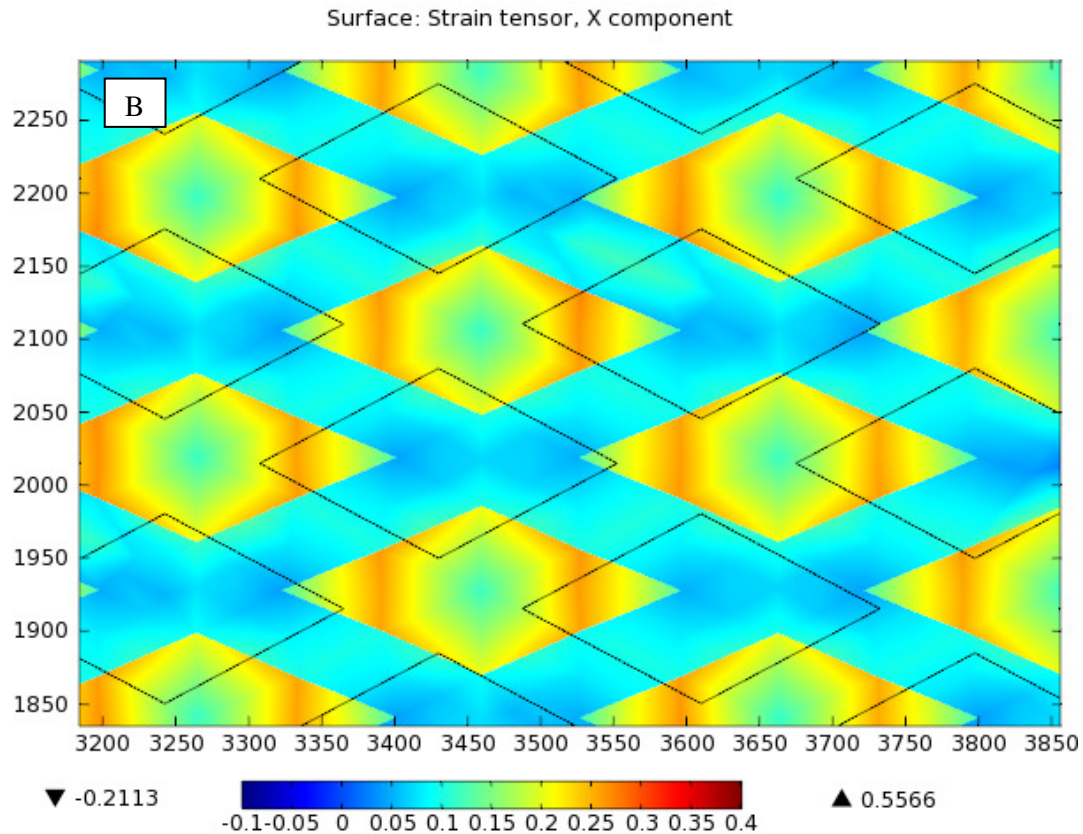


Figure 15: FE results of stress (A) and strain (B) distributions within cell seeded scaffold model and the overall deformation. Deformation can be seen in both the x and y directions. As the scaffold stretches in the x-direction, a displacement is seen in the y-direction (shrinking of the material) that accounts for the x displacement.

As seen in Figure 15, the model does assume a uniform tissue formation occurring within the pores. According to Figure 15, the stress was seen higher within the scaffold, but the strain was higher within the tissue. The assumption of uniform tissue formation is allowable with the model because experimentally, the goal is to construct a homogeneous cell-seeded scaffold that has uniform tissue formation similar to the native tissue. Before attempting to implant a TEHV, one would need to create a cell seeded scaffold which has uniform tissue formation and matches the FE results in overall composite stiffness and tissue stiffness. Since the tissue growth and ECM formation within the pores also increases the stiffness of the composite over time, the FE model can be used to predict tissue formation occurring over a period of cultivation time. Finally, since the stiffness of the tissue is dictated by collagen formation, the FE result for the E of the tissue can correlate to the collagen formation occurring in the composite.

Chapter 4: CONCLUSIONS, LIMITATIONS, AND FUTURE EXPERIMENTS

Through this study, we were able to model the structural mechanics of a PGS scaffold with uniform diamond shaped pores. The model was comparative to and supported experimental results. The correlation of the FE models to the experimental results was first shown to validate both the FE models and the experimental results since both produced similar stiffness values for the PGS scaffold. It was also shown that both the FE and experimental results showed linear trends in the stress-strain curves. Regarding the pore orientation, PD results showed a higher stiffness within the scaffold when compared to XD results. By modifying the geometry of the diamond pores, it was determined that scaffold anisotropy was dictated by the angle α of the pore when the volume fraction of the scaffold was maintained constant with the change in angle. The effects of the change in strut width were more evident when the angle was not near 90° . Finally, a cell-seeded model was made to predict the stiffness of the tissue formation occurring within the composite, which was 52.83 kPa when the overall stiffness was that of native bovine valvular tissue.

Within the FE modeling, there were various limitations. Overall, this model considered a uniform scaffold which had uniform porosity and pore geometry. Within the experimental phase, this was likely not the case as scaffold pore geometry and porosity can change based on the microfabrication process. Within the cell-seeded scaffold model, the tissue in the pores was also assumed to be uniform and the stiffness between pores constant within the model. This may also not be the case experimentally as the stiffness between the tissue formed in each pore can differ slightly depending on ECM formation. Regarding TEHV, the FE simulations showed that material selection of the synthetic scaffold needs to be highly considered and tested in order to design and construct a TEHV that has the mechanical properties and the biocompatibility of the native tissue.

For future experiments, work is currently being continued on the geometry of the scaffold to find an ideal geometry that would produce a stiffness in a cell seeded model that is close to that of native valvular tissue. The pore geometries are being changed to resemble various shapes such as a circle or square. The material properties of the scaffold are also being altered within the FE model based on other polymers such as poly lactic acid (PLA) and poly glycolic acid (PGA). Regarding other mechanical testing, the FE model is being used to analyze the ultimate tensile stress of the PGS scaffold and the strain to failure of the scaffold. These tests are being repeated in the composite cell seeded model. Once the FE analysis is done, experimental testing can be done on newly microfabricated scaffolds. Finally, *in vivo* testing of cell-seeded PGS scaffolds needs to be done to determine the immunological effects of the composite cell-seeded constructs.

REFERENCES

1. Rose JC, Hufnagel CA, Freis ED, Harvey WP, Partenoep EA., 1954. The Hemodynamic Alterations Produced By a Plastic Valvular Prosthesis For Severe Aortic Insufficiency in Man. *J Clin Invest* 33(6): 891–900.
2. Dasi LP, Simon HA, Sucosky P, Yoganathan AP, 2009. Fluid Mechanics of Artificial Heart Valves. *Clinical and Experimental Pharmacology and Physiology* 36: 225–237.
3. Cannegieter SC, Rosendaal FR, Briët E., 1994. Thromboembolic and bleeding complications in patients with mechanical heart valve prostheses. *American Heart Association. Circulation* 89:635-41.
4. Vesely I., 2005. Heart valve tissue engineering. *American Heart Association. Circulation* 97: 743–755.
5. Grunkemeier GL, Anderson WN., 1998. Clinical evaluation and analysis of heart valve substitutes. *J. Heart Valve Dis* 7: 163–9.
6. Mendelson K, Schoen F., 2006. Heart Valve Tissue Engineering: Concepts, Approaches, Progress, and Challenges. *Annals of Biomedical Engineering* 34: 1799-1819.
7. Engelmayr G.C. Jr., Sacks M.S., 2006. A structural model for the flexural mechanics of nonwoven tissue engineering scaffolds. *Journal of Biomechanical Engineering* 128(4), 610–622.
8. Engelmayr G.C. Jr., Sacks M.S., 2008. Prediction of extracellular matrix stiffness in engineered heart valve tissues based on nonwoven scaffolds. *Biomech Model Mechanobiol* 7:309–321.
9. Hammer PE, Sacks MS, Del Nido PJ, Howe RD.; 2011. Mass-Spring Model for Simulation of Heart Valve Tissue Mechanical Behavior. *Annals of Biomedical Engineering* 39 (6), 1668–1679.
10. Rabkin E, Schoen FJ., 2002. Cardiovascular tissue engineering. *Cardiovasc Pathol* 11(6):305–17.

11. Engelmayr, GC Jr., Rabkin E, Sutherland FW, Schoen FJ, Mayer JE Jr, Sacks MS.; 2005. The Independent Role of Cyclic Flexure in the Early In Vitro Development of an Engineered Heart Valve Tissue. *Biomaterials* 26(2), 175–187.
12. Weinberg EJ, Peter J. Mack PJ, Schoen FJ, Garcia-Cardena G, Mofrad MRK.; 2010. Hemodynamic Environments from Opposing Sides of Human Aortic Valve Leaflets Evoke Distinct Endothelial Phenotypes In Vitro. *Cardiovasc Eng* 10:5–11.
13. Jean A, Engelmayr GC.; 2010. Finite element analysis of an accordion-like honey comb scaffold for cardiac tissue engineering. *Journal of Biomechanics* 43:3035–3043.
14. Wang Y., Ameer G.A., Sheppard B.J., Langer R., 2002. A tough biodegradable elastomer. *Nature Biotechnology* 20(6), 602–606.
15. M.A.Hisham, et al., 2010. Analysis of Blood Flow into the Main Artery via Mitral Valve: Fluid Structure Interaction Model 356-360.

APPENDICES

Appendix A: Equations used by COMSOL Multiphysics

The following were equations used by COMSOL during the FE analysis of the models in this study (taken from the dynamic help within the COMSOL program).

The total strain tensor is written in terms of the displacement gradient

$$\varepsilon = \frac{1}{2}(\nabla \mathbf{u} + \nabla \mathbf{u}^T)$$

or in components as

$$\varepsilon = \frac{1}{2} \left(\frac{\partial u_m}{\partial x_n} + \frac{\partial u_n}{\partial x_m} \right)$$

Because of the symmetry, the strain tensor can be written as the following matrix:

$$\begin{bmatrix} \varepsilon_x & \varepsilon_{xy} & \varepsilon_{xz} \\ \varepsilon_{xy} & \varepsilon_y & \varepsilon_{yz} \\ \varepsilon_{xz} & \varepsilon_{yz} & \varepsilon_z \end{bmatrix}$$

Similar representation applies to the stress tensor:

$$\begin{bmatrix} s_x & s_{xy} & s_{xz} \\ s_{xy} & s_y & s_{yz} \\ s_{xz} & s_{yz} & s_z \end{bmatrix}$$

Due to the symmetry, the elasticity tensor can be completely represented by a symmetric 6-by-6 matrix as:

$$D = \begin{bmatrix} D_{11} & D_{12} & D_{13} & D_{14} & D_{15} & D_{16} \\ D_{12} & D_{22} & D_{23} & D_{24} & D_{25} & D_{26} \\ D_{13} & D_{23} & D_{33} & D_{34} & D_{35} & D_{36} \\ D_{14} & D_{24} & D_{34} & D_{44} & D_{45} & D_{46} \\ D_{15} & D_{25} & D_{35} & D_{45} & D_{55} & D_{56} \\ D_{16} & D_{26} & D_{36} & D_{46} & D_{56} & D_{66} \end{bmatrix} = \begin{bmatrix} c_{1111} & c_{1122} & c_{1133} & c_{1112} & c_{1123} & c_{1113} \\ c_{1122} & c_{2222} & c_{2233} & c_{2212} & c_{2223} & c_{2213} \\ c_{1133} & c_{2233} & c_{3333} & c_{3312} & c_{3323} & c_{3313} \\ c_{1112} & c_{2212} & c_{3312} & c_{1212} & c_{1223} & c_{1213} \\ c_{1123} & c_{2223} & c_{3323} & c_{1223} & c_{2323} & c_{2313} \\ c_{1113} & c_{2213} & c_{3313} & c_{1213} & c_{2313} & c_{1313} \end{bmatrix}$$

which is the elasticity matrix.

The Hooke's law can be presented then in the form involving the elasticity matrix and the following vectors:

$$\begin{bmatrix} s_x \\ s_y \\ s_z \\ s_{xy} \\ s_{yz} \\ s_{xz} \end{bmatrix} = \begin{bmatrix} s_x \\ s_y \\ s_z \\ s_{xy} \\ s_{yz} \\ s_{xz} \end{bmatrix}_0 + D \left(\begin{bmatrix} \epsilon_x \\ \epsilon_y \\ \epsilon_z \\ 2\epsilon_{xy} \\ 2\epsilon_{yz} \\ 2\epsilon_{xz} \end{bmatrix} - \begin{bmatrix} \epsilon_x \\ \epsilon_y \\ \epsilon_z \\ 2\epsilon_{xy} \\ 2\epsilon_{yz} \\ 2\epsilon_{xz} \end{bmatrix}_0 - \theta \begin{bmatrix} \alpha_x \\ \alpha_y \\ \alpha_z \\ 2\alpha_{xy} \\ 2\alpha_{yz} \\ 2\alpha_{xz} \end{bmatrix} \right)$$

Thus, the general conversion rule for indices is:

$$\begin{bmatrix} 11 \\ 22 \\ 33 \\ 12, 21 \\ 23, 32 \\ 13, 31 \end{bmatrix} \leftrightarrow \begin{bmatrix} 1 \\ 2 \\ 3 \\ 4 \\ 5 \\ 6 \end{bmatrix} \leftrightarrow \begin{bmatrix} x \\ y \\ z \\ xy \\ yz \\ xz \end{bmatrix}$$

COMSOL Multiphysics uses the complete tensor representation internally to perform the coordinate system transformations correctly.

In the most general case of fully anisotropic material, you provide explicitly 21 components of the symmetric elasticity matrix D and 6 components of the symmetric thermal expansion matrix.

In this case for isotropic material and elastic moduli, the elasticity matrix becomes:

$$D = \frac{E}{(1+\nu)(1-2\nu)} \begin{bmatrix} 1-\nu & \nu & \nu & 0 & 0 & 0 \\ \nu & 1-\nu & \nu & 0 & 0 & 0 \\ \nu & \nu & 1-\nu & 0 & 0 & 0 \\ 0 & 0 & 0 & \frac{1-2\nu}{2} & 0 & 0 \\ 0 & 0 & 0 & 0 & \frac{1-2\nu}{2} & 0 \\ 0 & 0 & 0 & 0 & 0 & \frac{1-2\nu}{2} \end{bmatrix}$$

Appendix B: Step-by-Step FE Model Explanation

- I. Defining the Space Dimension
 - a. Start COMSOL multiphysics
 - b. Model wizard
 - c. Select space dimension
 - i. 2-D
 - ii. Click on “next” arrow
- II. Defining the Physics
 - a. Add physics
 - b. Structural mechanics
 - c. Solid mechanics
- III. Defining the Study Type
 - a. Select study type
 - b. Preset studies
 - c. Stationary
 - d. Click on the “finish” flag
- IV. Defining the Geometry
 - a. Making global variables
 - i. Right click global definitions
 - ii. Parameters
 - iii. Add parameter L1, H1, L2, and H2 for pore dimensions (see Figure 2, note no unit is necessary)
 - b. Making the one pore
 - i. Click geometry
 - ii. Length unit
 1. μm
 - iii. Right click on geometry
 - iv. Polygon
 - v. $x = \{0, L1, 2 * L1, L1, 0\}$
 - vi. $y = \{H1, 2 * H1, H1, 0, H1\}$
 - c. Copying the pore
 - i. Right click on geometry
 - ii. Transforms
 - iii. Copy
 - iv. Add pol1

- v. $x = L1+L2$
 - vi. $y = H1+H2$
 - vii. Right click on geometry
 - viii. Boolean operators
 - ix. Union
 - x. Add pol1 and copy 1
- d. Making array of pores
- i. Right click on geometry
 - ii. Transforms
 - iii. Array
 - iv. Add uni1
 - v. Array type linear
 - vi. Size 50
 - vii. $x \text{ disp} = 2*L1+2*L2$
 - viii. $y \text{ disp} = 0$
 - ix. Right click on geometry
 - x. Boolean operators
 - xi. Union
 - xii. Add all objects
 - xiii. Right click on geometry
 - xiv. Transforms
 - xv. Array
 - xvi. Add uni2
 - xvii. Array type linear
 - xviii. Size 60
 - xix. $x \text{ disp} = 0$
 - xx. $y \text{ disp} = 2*H1+2*H2$
 - xxi. Right click on geometry
 - xxii. Boolean operators
 - xxiii. Union
 - xxiv. Add all objects
- e. Making the rectangular scaffold
- i. Right click on geometry
 - ii. Rectangle
 - iii. Size is width 7000 height 4000
 - iv. Position $x = L1+10$

- v. Position $y = H1$
 - f. Cutting out pores from scaffold
 - i. Right click on geometry
 - ii. Boolean operators
 - iii. Difference
 - iv. Add r1 to objects to add
 - v. Add uni3 to objects to subtract
 - vi. Choose “build all” in the top right hand corner
 - vii. Note for cell seeded model the pore scaffold is first made as described above, then the tissue filling the pores is made using the same geometry but using an array that fits the scaffold pores
- V. Setting Up Integration Function for Volume Fraction Calculation
 - a. Right click definitions
 - b. Model couplings
 - c. Integration
 - d. Add 1 to selection
 - e. Right click definitions
 - f. Variables
 - g. Name = surfarea
 - h. Expression = $\text{intop1} (1*1)$
- VI. Specifying the Material Properties
 - a. Material properties
 - b. Right click on materials
 - c. Material
 - d. Basic
 - e. Output properties
 - f. Density
 - g. Click add
 - h. Poisson’s ratio
 - i. Click add
 - j. Young’s modulus
 - k. Click add
 - l. Density = 1235 kg/m³
 - m. Poisson’s ratio = 0.49
 - n. Young’s modulus = 1.77 MPa

- o. Note for cell seeded model, a second material property is given to the tissue > Density = 1060 kg/m³ > Poisson's ratio = 0.49 > Young's modulus = (30, 43, 60, 90, 120) kPa

VII. Specifying Initial Conditions

- a. Right click solid mechanics
- b. Fixed constraint
- c. Select all left boundary of model and add
- d. Right click solid mechanics
- e. Boundary load
- f. Select all right boundary of model and add
- g. Load type is load as a force per unit area
- h. $x = (0.05, 0.1, 0.2, 0.3) \text{ N/m}^2$
- i. $y = 0 \text{ N/m}^2$

VIII. Specifying the Mesh

- a. Right click mesh
- b. Free triangular
- c. Click size
- d. Element size
- e. Custom
- f. Max element size = 400
- g. Min element size = 2.1
- h. Max element growth rate = 1.3
- i. Resolution of curvature = 0.3
- j. Resolution of narrow regions = 1
- k. Note this mesh is similar to a predefined fine mesh and was used for the entire geometry in all models

IX. Running the Study and Characterizing the Results

- a. Keep study 1 parameters as default
- b. To compute, right click study
- c. Compute (“=” sign on menu)
- d. Report automatically displays, if not right click results
 - i. 2-D plot
 - ii. Right click 2-D plot
 - iii. Surface
 - iv. Expression is either von Mises stress or strain in the x-direction depending on which distribution is being measured

- e. For stain determination of overall scaffold, right click derived values
 - i. Point evaluation
 - ii. Select 5 point on the right edge (toward center of the edge)
 - iii. Expression is displacement in the x-direction
 - iv. Average these displacements and divide by $7000\mu\text{m}$ to calculate the strain
- f. For volume fraction
 - i. Right click results
 - ii. 1-D plot
 - iii. Right click 1-D plot
 - iv. Global
 - v. Data set is from parent
 - vi. Expression = surfarea
 - vii. Right click 1-D plot
 - viii. Histogram
 - ix. Expression = surfarea
 - x. Find the peak of the histogram to find the surface area of the scaffold and multiply by 0.25mm thickness to find V_{pgs}
 - xi. Volume fraction = $V_{\text{pgs}}/V_{\text{total}}$ where $V_{\text{total}} = 7\text{mm} * 4\text{mm} * 0.25\text{mm}$

Appendix C: FE Results with Meshing

Table A1: Raw data of scaffold stiffness for geometry testing experiments. The stiffness was calculated from the slope of the linear trend line to the stress-strain curves for each model. Strain was measured in the models as described in the methods section of this thesis. This data was used to produce Figure 12.

Strut Width (w)	Angle (α) Degrees	Young's Modulus PD	Young's ModulusXD	EPD/EXD
35	30	0.566	0.002	283.000
	45	0.338	0.008	42.250
	65	0.201	0.031	6.484
	90	0.097	0.105	0.924
50	30	1.541	0.005	308.200
	45	0.597	0.022	27.136
	65	0.366	0.082	4.463
	90	0.173	0.172	1.006
60	30	1.467	0.014	104.786
	45	0.863	0.029	29.759
	65	0.728	0.104	7.000
	90	0.244	0.297	0.822
70	30	1.170	0.013	90.008
	45	1.342	0.043	31.209
	65	0.676	0.123	5.496
	90	0.300	0.300	1.000

Figures A1 and A2 show the meshing, strain, and stress distributions for a scaffold with a pore angle α of 30° and strut width of $60 \mu\text{m}$. Figures A3 and A4 show the meshing, strain, and stress distributions for a scaffold with a pore angle α of 65° and strut width of $60 \mu\text{m}$. Figures A1 and A2 show the meshing, strain, and stress distributions for a scaffold with a pore angle α of 65° and strut width of $70 \mu\text{m}$. Notice that the free-triangular mesh became denser as the angle α decreased (difference between Figure A1 and A3). The mesh also became denser as the strut width decreased (difference between Figure A3 and A5).

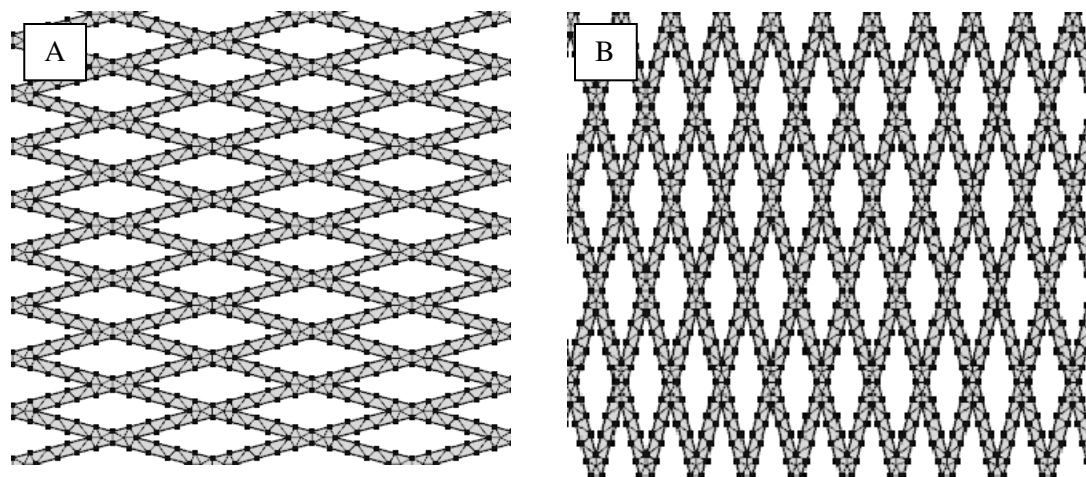
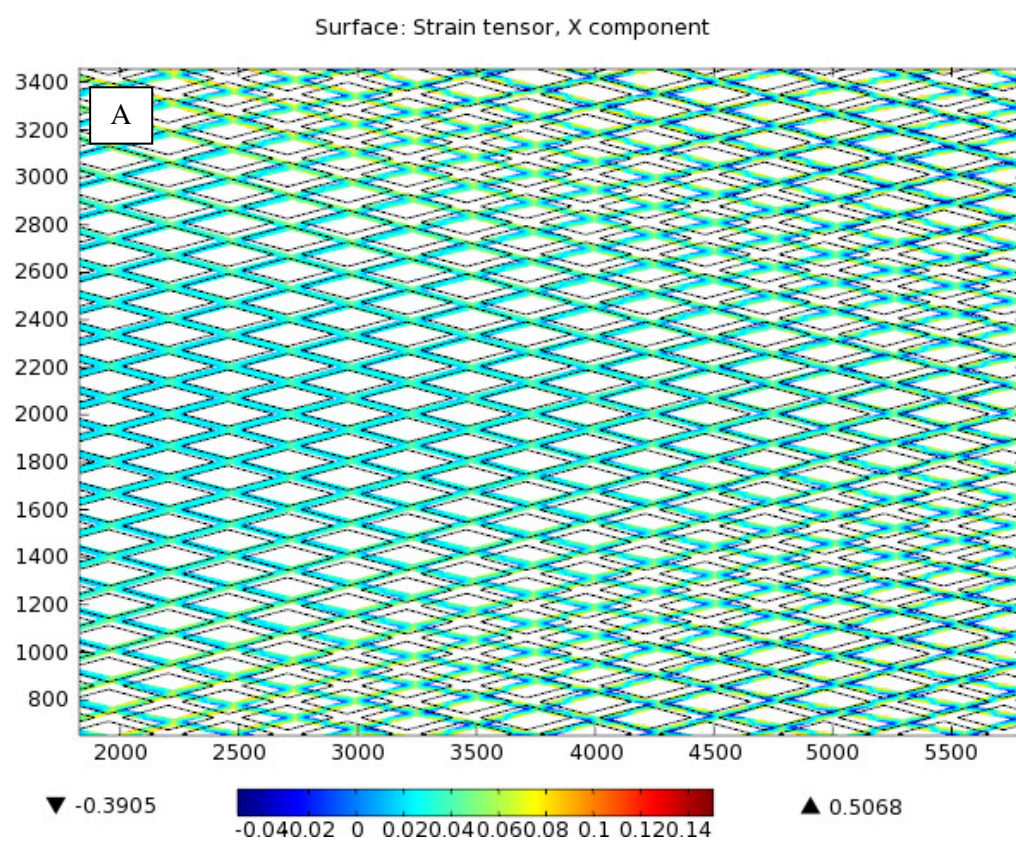


Figure A1: Meshing images of center of scaffold for pore geometry with angle α of 30° and strut width of $60\ \mu\text{m}$.



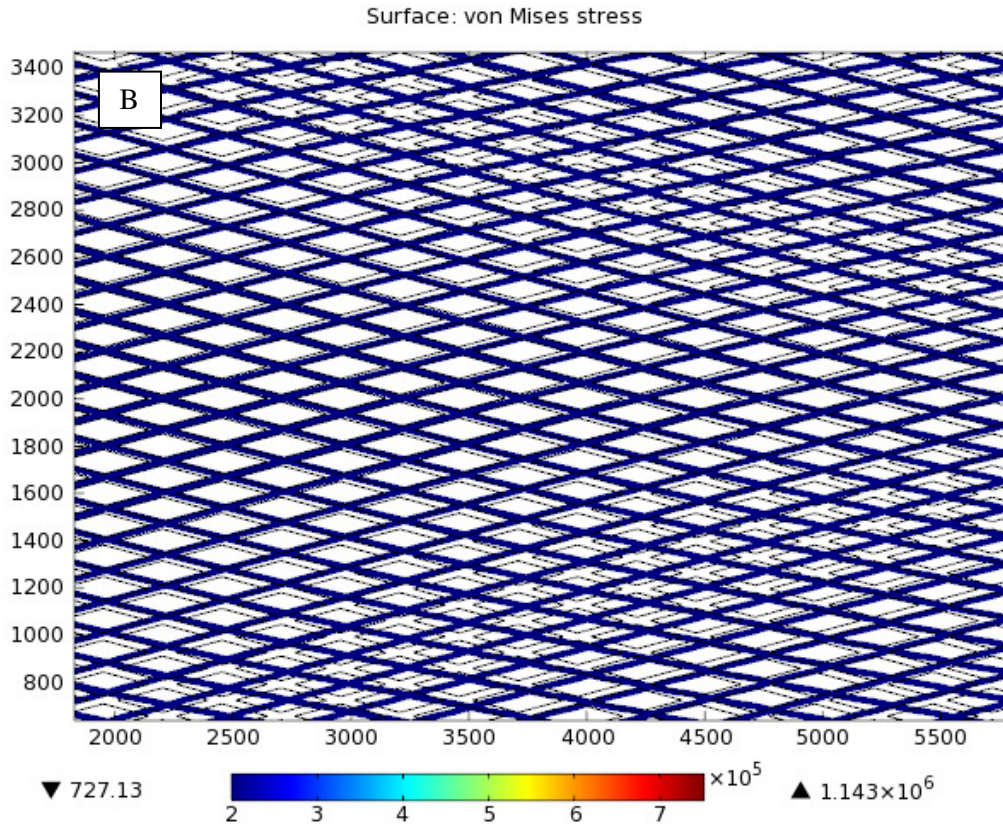


Figure A2: Strain (A) and stress (B) distributions for scaffold stretched by a 0.1 MPa load for pore geometry with angle α of 30° and strut width of $60\ \mu\text{m}$. Images are taken of scaffold's center.

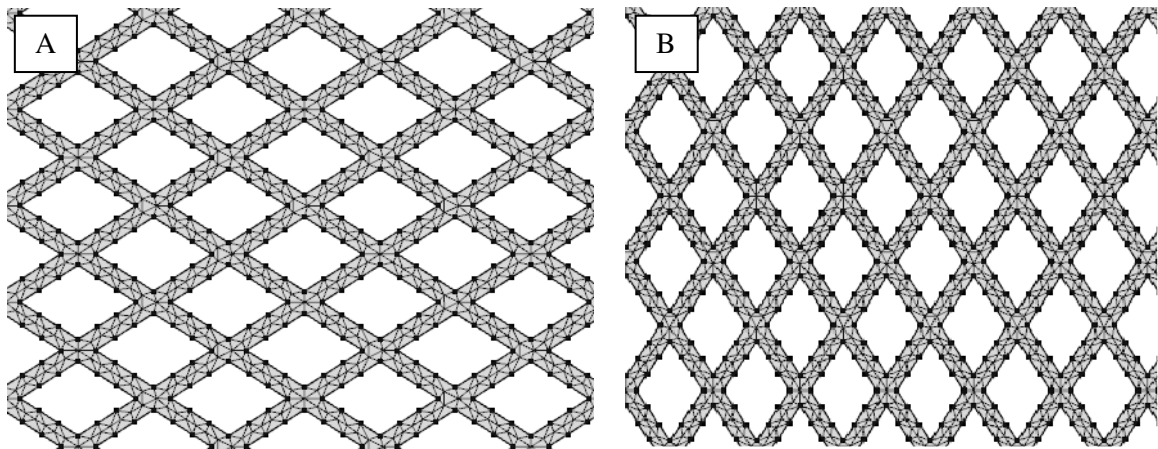
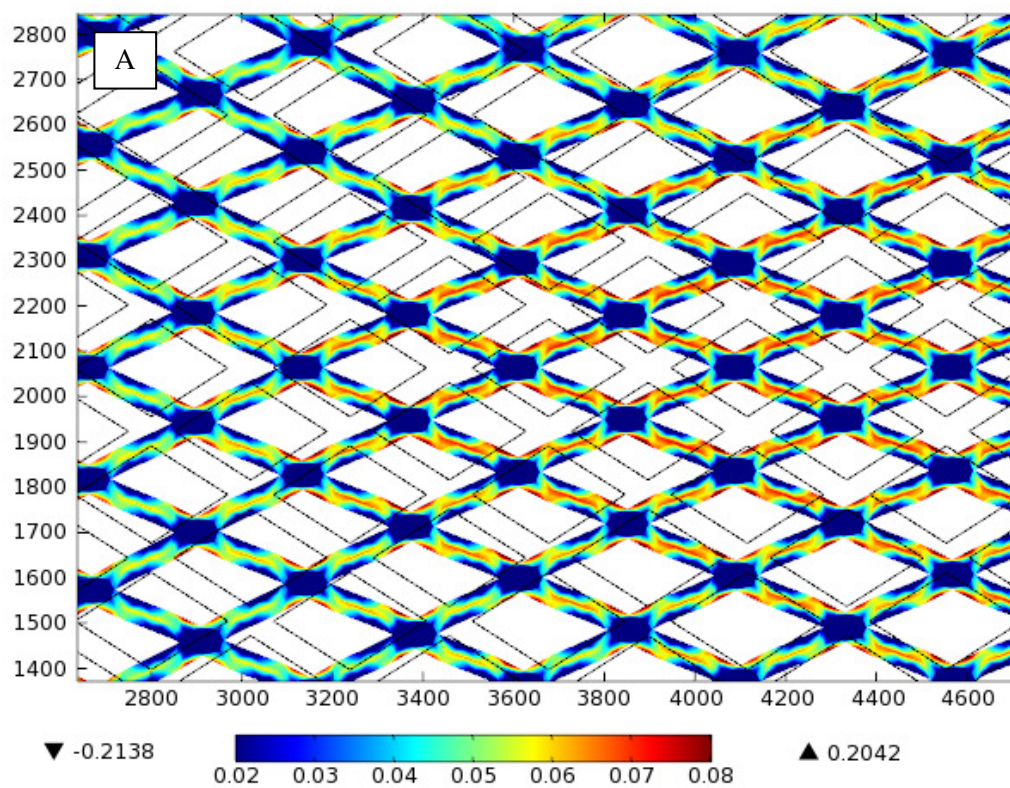


Figure A3: Meshing images of center of scaffold for pore geometry with angle α of 65° and strut width of $60\ \mu\text{m}$.

Surface: Strain tensor, X component



Surface: von Mises stress

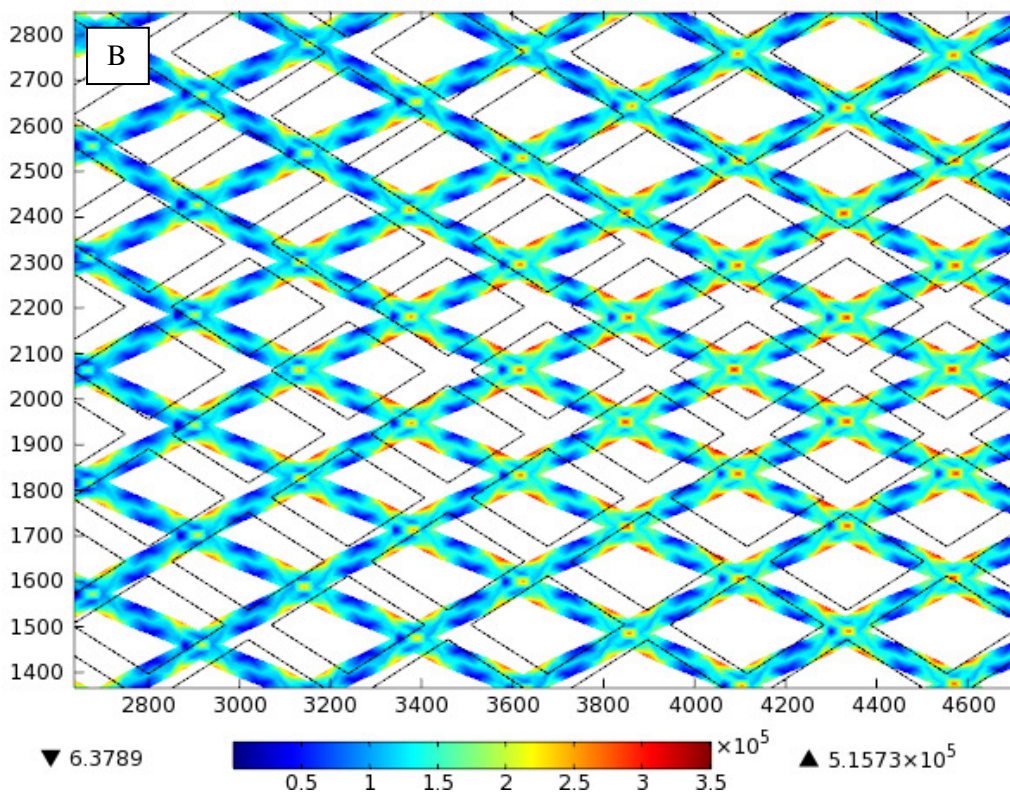


Figure A4: Strain (A) and stress (B) distributions for scaffold stretched by a 0.1 MPa load for pore geometry with angle α of 65° and strut width of $60\ \mu\text{m}$. Images are taken of scaffold's center.

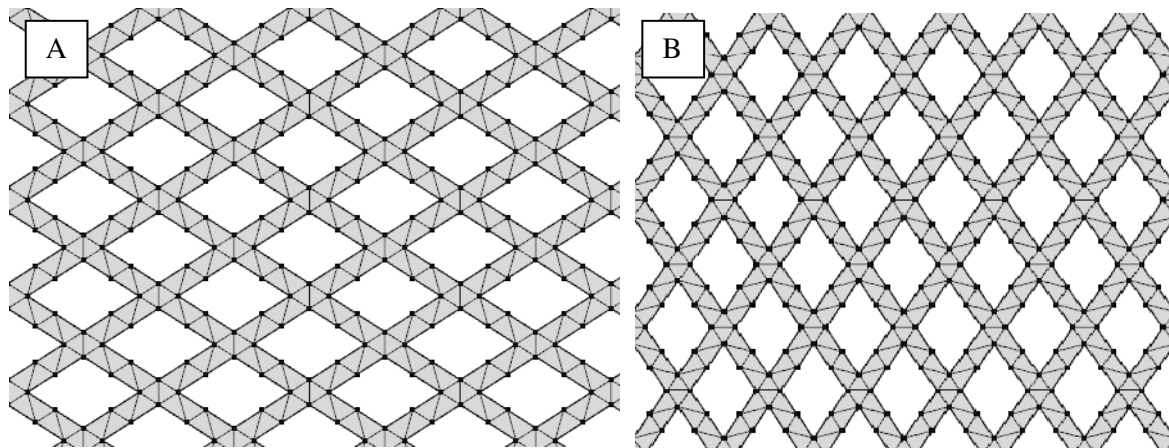
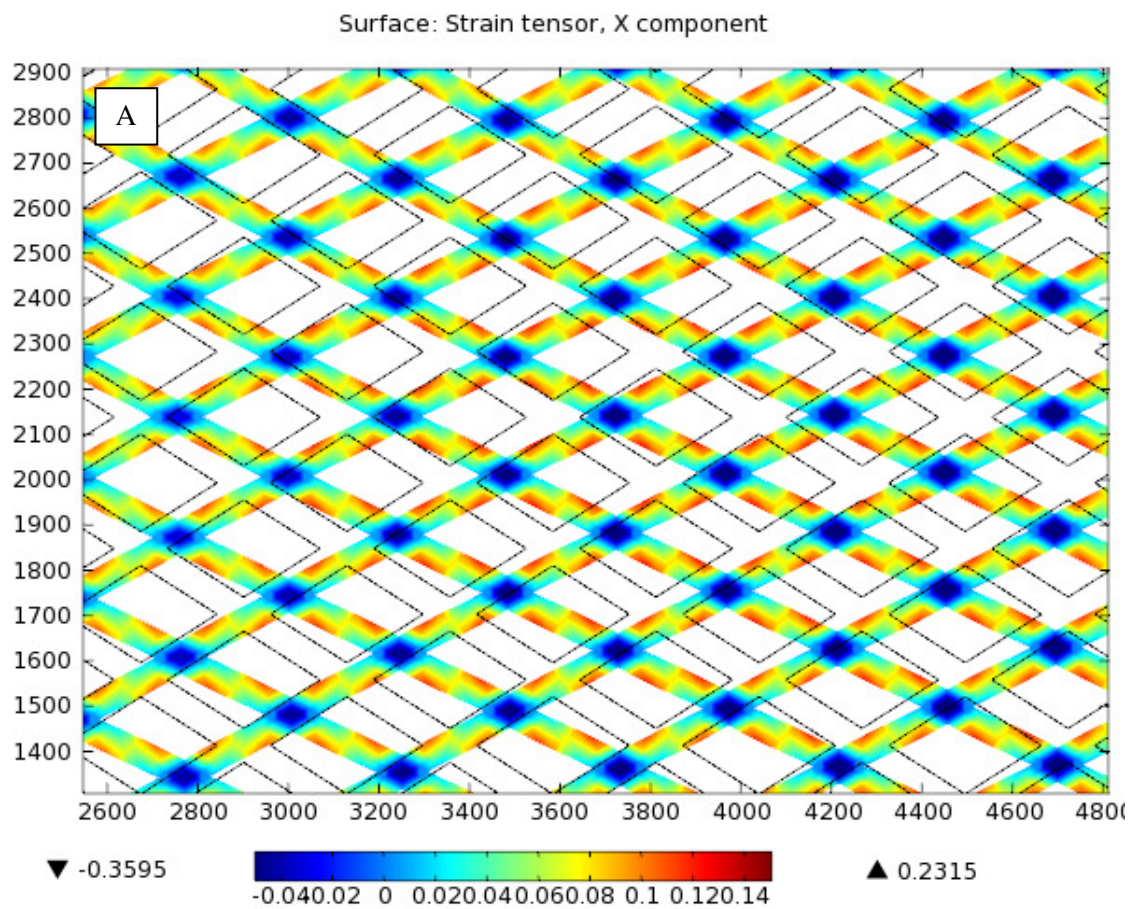


Figure A5: Meshing images of center of scaffold for pore geometry with angle α of 65° and strut width of $70\ \mu\text{m}$.



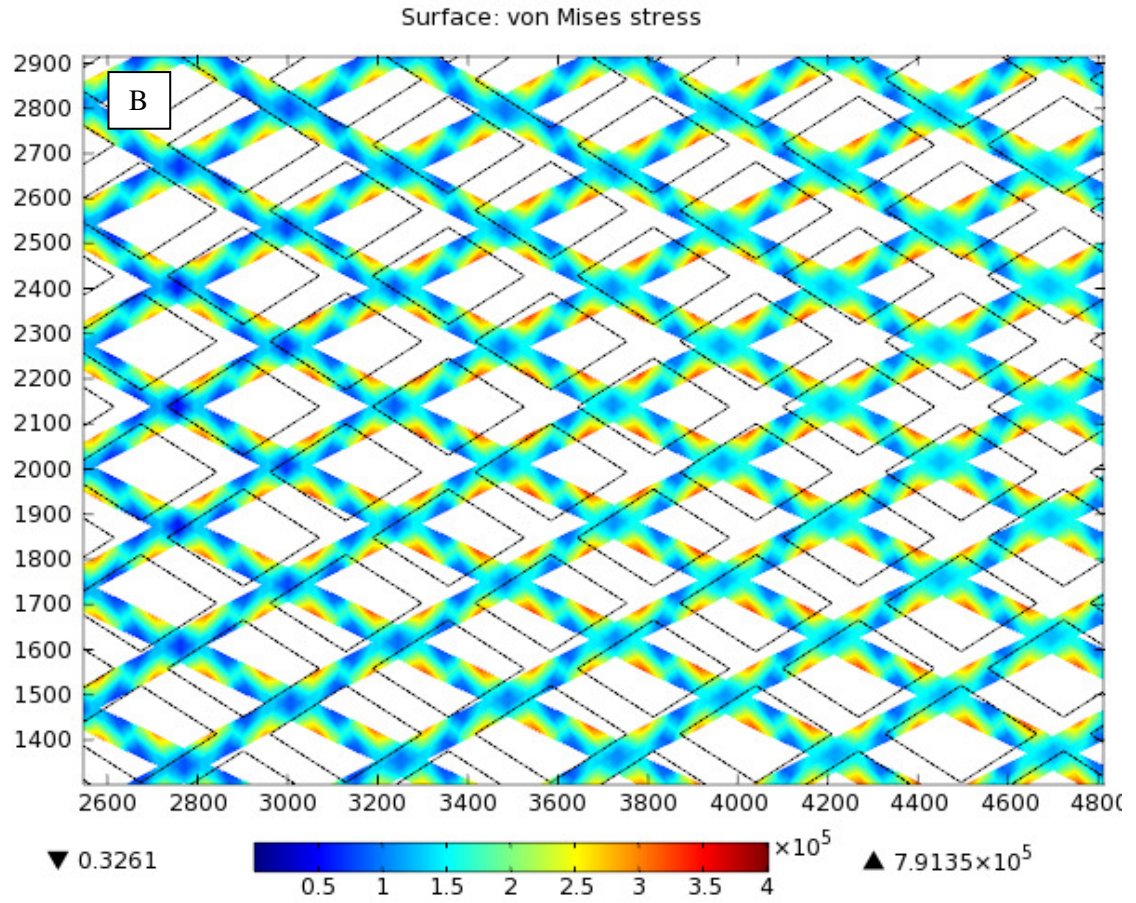


Figure A6: Strain (A) and stress (B) distributions for scaffold stretched by a 0.1 MPa load for pore geometry with angle α of 65° and strut width of $70\ \mu\text{m}$. Images are taken of scaffold's center.

ACADEMIC VITA: SURJYANIL CHOWDHURY

QUALIFICATIONS PROFILE

Motivated professional with excellent organizational and collaboration skills. Ideal candidate for a position requiring drive, initiative, responsibility, and innovation. Demonstrates stellar leadership qualifications in creating and managing a small startup company as well as leading a college level class. Proficient in various computer aided design, simulation, and Microsoft Office tools. Seeking full-time position in engineering following May 2012 graduation.

RELEVANT COURSES

- | | | |
|-----------------------------|-------------------------------|------------------------------|
| ➤ Surfaces and Biomaterials | ➤ Reaction Kinetics | ➤ Biomedical Instrumentation |
| ➤ Tissue Engineering | ➤ Continuum & Fluid Mechanics | ➤ Biothermodynamics |
| ➤ Regenerative Medicine | ➤ Mass Transport Phenomena | ➤ Organic Chemistry |
-

EMPLOYMENT HISTORY

TEACHING ASSISTANT

AUG 2010 – PRESENT

PENN STATE DEPARTMENT OF BIOLOGY ■ UNIVERSITY PARK, PA

- ⊙ Instruct multiple physiology laboratory classes consisting of 16 or more students each
- ⊙ Conduct pre-laboratory and post-laboratory discussions and concept reviews
- ⊙ Evaluate students' class work by grading exams, quizzes, and laboratory reports

BRANCH MANAGER/ENTREPRENEUR

FEB 2011 - AUG 2011

COLLEGEWORKS PAINTING ■ PHILADELPHIA, PA

- ⊙ Developed and built a painting business from the ground up in the Philadelphia and Glenside areas
- ⊙ Hired and managed multiple teams comprised of 7 marketing personnel and 17 painters
- ⊙ Implemented business marketing plans using various advertisement and direct marketing techniques
- ⊙ Planned and executed 15 projects which generated more than \$40,000 in revenue with a 20% profit margin
- ⊙ Streamlined communication between clients and employees which improved employee accountability

MINORITY UNDERGRADUATE STUDENT INTERNSHIP PROGRAM

JUNE 2010 - AUGUST 2010

INTERN

U.S. ARMY, EDGEWOOD CHEMICAL BIOLOGICAL CENTER ■ EDGEWOOD, MD

- ⊙ Expressed a G-type nerve agent degrading enzyme (OPAA) in various strains of *Escherichia coli*
- ⊙ Isolated OPAA proteins and assessed expression using SDS-PAGE analysis
- ⊙ Quantified enzyme kinetics using UV/Vis and optical density readings
- ⊙ Presented research to the board of directors and fellow co-workers

UNDERGRADUATE RESEARCHER

JUN 2009 – AUG 2009

HANCOCK LABORATORY, MOLECULAR BIOMECHANICS ■ UNIVERSITY PARK, PA

- ⦿ Conduct bioengineering research focusing on kinesin mechanics and transport
- ⦿ Examine kinesin velocities and stepping rates using microtubule gliding assays
- ⦿ Assess adenosine triphosphate hydrolysis effects on kinesin motor processivity through single-molecule studies
- ⦿ Analyze single motor stepping using total internal reflection fluorescence and epifluorescence microscopy
- ⦿ Quantify active motor concentrations using spectrofluorimeter analysis

EDUCATION

BACHELOR OF SCIENCE IN BIOENGINEERING

Schreyer Honors College, Pennsylvania State University, University Park PA, Expected Graduation: May 2012

ADDITIONAL QUALIFICATIONS

TECHNICAL SKILLS: MATLAB | Simulink | Microsoft Office Suite 2007 | Origin 8 | Minitab

COMPUTER AIDED DESIGN SOFTWARE: COMSOL | LabVIEW | Solid Works | Google SketchUp

LANGUAGES: Fluent in English and regional Indian language: Bengali